THE ASTROPHYSICAL JOURNAL, 388:648–668, 1992 April 1

THE ABUNDANCE AND DISTRIBUTION OF WATER VAPOR IN THE JOVIAN TROPOSPHERE AS INFERRED FROM *VOYAGER* IRIS OBSERVATIONS

BARBARA E. CARLSON, ANDREW A. LACIS, AND WILLIAM B. ROSSOW
Goddard Space Flight Center Institute for Space Studies, New York, NY 10025
Received 1990 August 31; accepted 1991 October 8

ABSTRACT

We have reanalyzed the *Voyager* IRIS spectra of the Jovian North Equatorial Belt (NEB) hot spots using a radiative transfer model which includes the full effects of anisotropic multiple scattering by clouds. The atmospheric model includes the three thermochemically predicted cloud layers, NH_3, NH_4SH, and H_2O. Spectrally dependent cloud extinction is modeled using Mie theory and the refractive indices of NH_3 ice, NH_4SH ice, water, and H_2O ice. The upper tropospheric temperature profile, gas abundances, height-dependent para-hydrogen profile, and vertical distribution of NH_3 cloud opacity are retrieved from an analysis of the far-infrared (180–1200 cm^{-1}) IRIS observations. With these properties constrained, the 5 μm (1800–2300 cm^{-1}) observations are analyzed to determine the atmospheric and cloud structure of the deeper atmosphere ($P > 1.5$ bars). Since the NEB hot spots correspond to regions of minimum cloud opacity, these observations allow us to probe the atmosphere down to the ≈ 5 bar level. The results show that the abundance of water is *at least* 1.5 times solar with 2 times solar (2.76×10^{-3} mixing ratio relative to H_2) providing the best-fit to the *Voyager* IRIS hot spot observations. We then use IRIS observations of the Tropical and Equatorial regions to examine spatial variations in relative humidity. Our results show that regions with average 5 μm brightness temperatures in excess of 230 K are areas of reduced relative humidity, while colder regions are best-fit with a saturated water profile.

Subject headings: planets and satellites: individual (Jupiter)

1. INTRODUCTION

Determination of the abundance of water vapor on Jupiter is of fundamental importance for understanding the basic planetary structure, dynamics, and early evolution of the Jovian atmosphere. Water vapor was first detected by Larson et al. (1975). Their preliminary analysis suggested a mixing ratio of $\approx 10^{-6}$ associated with a temperature in excess of 300 K and a pressure less than 20 bars, suggesting that water deep in Jupiter's hot spots is responsible for the lines observed in 5 μm airborne spectrum. Earlier analyses of the *Voyager* IRIS 5 μm observations also implied that water is greatly depleted on Jupiter (Kunde et al. 1982; Drossart & Encrenaz 1982; Bjoraker, Larson, & Kunde 1986a; Lellouch, Drossart, & Encrenaz 1989) by nearly a factor of 50 compared to the solar mixing ratio of 1.38×10^{-3} (Cameron 1982), referenced here with respect to H_2. Bjoraker et al. (1986a) also analyzed the Kuiper airborne spectrum and obtained results that are consistent with their analysis of the spatially resolved *Voyager* IRIS observations. These results are puzzling because they contradict expectations based on interior structure models, equilibrium chemical models, chemical kinetic models and dynamical models of the Jovian atmosphere.

Interior stucture models, optimized to match the measured gravitational harmonics, imply the existence of some abundant heavy species and suggest that the composition of Jupiter is nearly solar (Hubbard & Marley 1989). Furthermore, the bulk abundances of the heavy elements (e.g., C, N, O, and S) are constrained only to be less than 10–20 times solar by measurements of the gravitational moments of Jupiter (Stevenson 1982). Equilibrium chemistry models of the Jovian atmosphere suggest that the abundance of water is solar to supersolar (Fegley & Prinn 1988; Carlson, Prather, & Rossow 1987) while chemical kinetic models of CO, constrained by the observed abundance of CO (Noll et al. 1988), require near solar abundances of water (Prinn & Barshay 1977). Moist convection models suggest that only solar amounts of water would have enough latent heat to trigger the observed equatorial plumes (Del Genio & McGrattan 1990), while models of the equatorial wave structure require supersolar abundances of water to support the vertical eigenmode structure of the equatorial waves (Allison 1990). We present a reanalysis of the *Voyager* IRIS 5 μm observations which shows that the abundance of water on Jupiter is enhanced by a factor of at least 1.5 times solar, with 2 times the solar abundance of water providing the best fit to the observations.

We focus our study on the 5 μm hot spots within the North Equatorial Belt (NEB). As in previous analyses, we employ the same brightness temperature criteria used by Kunde et al. (1982) to select the hottest 5 μm spectra. Since these spectra correspond to regions of minimum cloud opacity (Carlson, Lacis, & Rossow 1991a, b), they are most sensitive to the gas composition and cloud structure of the deep troposphere.

While our approach to modeling gas opacity is similar to that used in previous investigations (i.e., direct spectral line-by-line integration), our treatment of cloud extinction, scattering, and thermal emission is fundamentally different (Carlson, Lacis, & Rossow 1991a). Previous investigators (e.g., Kunde et al. 1982; Bjoraker et al. 1986a; Lellouch et al. 1989) used a *single* gray-absorbing cloud to reduce their gas-only model continuum to match the IRIS observations. Instead, we infer the properties of a thermochemically consistent set of clouds from the entire IRIS spectrum and use Mie theory, in conjunction with the refractive indices of NH_3 ice, NH_4SH ice, water, and H_2O ice, to calculate the spectral dependence of cloud extinction and emission for each cloud type, including the effects of scattering as well as absorption and emission. The

doubling and adding method is used to model the effects of overlapping gaseous absorption, anisotropic multiple scattering, and thermal emission from each of these clouds in a multilayered inhomogeneous atmosphere. In other words, the cloud radiative properties are decidedly nongray and it is this difference which alters conclusions regarding the retrieved H_2O abundance.

Motivation to reanalyze the *Voyager* IRIS 5 μm observations is threefold. First, in none of the previous analyses has the cloud structure assumed in the retrieval model been thermochemically consistent with the inferred water abundance or the assumed abundances of the other condensible species. Second, for the same set of observations, two separate analyses (Kunde et al. 1982 and Bjoraker et al. 1986a, hereafter K82 and BLK, respectively) reported a 2 bar difference in the pressure levels assigned to the retrieved water abundances. Third, there is no known physical mechanism capable of producing the inferred order of magnitude decrease in water abundance in the pressure regime from 4 to 6 bars in the case of BLK, and from 2 to 4 bars in the case of K82, since these regions are found to lie below the expected condensation level of water vapor (also see discussion in Del Genio & McGrattan 1990).

Marten et al. (1981) demonstrated that NH_3 cloud extinction alone cannot be responsible for the observed spatial variation in 5 μm brightness temperatures. While the observed variation is of order a few tens of degrees, they found that NH_3 cloud extinction can, at most, account for 14° C of the observed brightness temperature variation. Their analysis of the far-infrared observations implied that at least one additional cloud layer must be present in the Jovian atmosphere and that this cloud was located at pressures greater than 1.5 bars.

Bézard, Baluteau, & Marten (1983) investigated the deeper cloud structure of the Jovian atmosphere using IRIS observations of the equatorial region. They defined four spectral ensembles based on 5 μm brightness temperature selection criteria and used their hottest spectral ensemble as a proxy for a clear gas synthetic spectrum. They then used a gray-absorbing cloud to attenuate the spectral radiance of the hottest ensemble to match the continuum level of the other IRIS observations. Though unable to reproduce the observations comprising their colder spectral ensembles, they nevertheless were able to determine the approximate location, in terms of effective temperature, of the cloud layer responsible for most of the observed 5 μm brightness temperature variation: they concluded that the dominant source of 5 μm continuum opacity is a cloud located at roughly 190–210 K ($P \approx 2$ bars). The location of this second cloud layer compared with the results of thermochemical equilibrium models (e.g., Weidenschilling & Lewis 1973) suggested NH_4SH as its likely composition.

It is important to remember that analyses of the NEB hot spot observations (e.g., K82) have demonstrated that some cloud opacity is required in hot spots to lower the gas-only model continuum level to that of the observations. Furthermore, since Bézard et al. (1983) did not model gaseous absorption or emission, their gray-absorbing cloud is, in terms of its effect on the radiation, located at the top of the atmosphere, regardless of its effective temperature, and therefore does not interact with the gaseous spectrum except in a greatly simplified manner. We show that, in this special case, the gray-absorbing cloud can act as a neutral density filter and not alter line-to-continuum ratios, provided that the Planck emission from the cloud is negligible (i.e., it is cold relative to the gas emission temperature).

Thus, the analyses of the *Voyager* IRIS data by Marten et al. (1981) and Bézard et al. (1983) imply at least two clouds in the Jovian atmosphere. More recently, Gierasch, Conrath, & Magalhães (1986) also confirmed that at least two spectrally distinct cloud layers are required, one correlated strongly with the ammonia abundance and detectable at both 5 and 45 μm and the other more uniformly distributed and detectable only at 5 μm. Despite this evidence for a multilayered cloud structure that affects the 5 μm spectrum, all previous gas abundance retrievals using the *Voyager* IRIS 5 μm observations have included only a single absorbing cloud layer located near the expected NH_4SH cloud level.

Since water can condense in the Jovian atmosphere, the notion that a low retrieved water abundance reflects a bulk depletion depends critically on the pressure level ascribed to the measurement. For example, a mole fraction of 3×10^{-5} in the deep atmosphere at 6 bars, as retrieved by BLK, implies that water is depleted by a factor of 46 with respect to solar, while the same abundance at 2.3 bars merely reflects saturated vapor conditions, which provide only a lower limit on the well-mixed abundance. Hence, our second reason to reanalyze the 5 μm data stems from the inconsistency in the results obtained by K82 and BLK for the same subset of the IRIS observations, namely NEB hot spots. In the K82 analysis, the absorbing cloud is modeled as a diffuse haze distributed throughout the line-forming region (2 to 4 bars) with a total column optical depth of 0.54. The K82 model also includes an arbitrary, optically thick lower boundary at 5 bars (279 K). With this model, K82 inferred a water profile varying from 3×10^{-5} at 4 bars to 1×10^{-6} at 2.5 bars.

In the BLK analysis, an absorbing cloud with an optical depth of 2.93 is placed at 2 bars (210 K), which is above the line-forming region; hydrogen opacity, extending to 12 bars (353 K), provides the optically thick lower boundary. With this model, BLK inferred a water profile varying from 3×10^{-5} at 6 bars to 4×10^{-6} at 4 bars. Note that the inferred water abundances are almost identical to those retrieved by the K82 analysis, but that differences in model lower boundary conditions, cloud opacities, and locations lead to a 2 bar difference in the pressure levels to which the retrieved water abundances are assigned. Even in the case of a pure gas atmosphere, there is a difference of 2 bars in the pressure level of unit optical depth calculated in these two studies, which can only be attributable to differences in the lower boundary condition, since both studies use the same spectrum synthesis program developed by Kunde & Maguire (1974) to model the gas transmittance.

Lellouch et al. (1989, henceforth LDE) assumed a constant mixing ratio of water below the 230 K ($\approx$2.5 bars) level with a sharp cutoff above this level. To reduce their synthetic continuum to match that of the IRIS observations, LDE included an absorbing cloud at the 200 K level ($\approx$2 bars), the optical depth of which was a free parameter. With this model, they concluded that the cloud in NEB hot spots has an optical depth of $\approx$0.8, while in colder spectral ensembles within the NEB, for which the average 5 μm brightness temperature was less than 230 K, they retrieved a cloud optical depth of 2.3. The deep mixing ratio of water was found to vary from 2.0×10^{-6} in the NEB hot spots to 2.4×10^{-5} in the colder spectral ensembles.

The inferred variations in water vapor profile in the LDE study, as well as in the BLK and in the K82 analyses, are all found to occur *below* the respective levels of water vapor saturation (or condensation), where a uniformly mixed vapor profile is expected. No physical mechanisms are suggested in

these studies that might explain the order of magnitude variation in water vapor abundance within the deep atmosphere below the condensation level. Thus, our third reason to reanalyze the 5 μm data stems from the ad hoc nature of the water vapor distributions that are used in the previous studies to explain the spectral variations in the 5 μm IRIS data.

2. THE RADIATIVE TRANSFER MODEL

Our procedure for analyzing the Jovian IRIS spectra is a standard radiative transfer comparison of synthetic spectra with the *Voyager* observations; however, we model the entire IRIS spectrum rather than limited sections to constrain the atmospheric and cloud properties as much as possible (Carlson et al. 1991a). The synthetic spectra are judged to provide a good fit to the data when they fit the observations to within the standard deviation of the spectra comprising the average *Voyager* spectrum. This yields a fit to the average Jovian cloud structure corresponding to that subset of the IRIS observations and provides a measure of the spatial inhomogeneity of the Jovian atmosphere.

2.1. *Calculation of the Molecular Opacity*

Line-by-line calculations are performed using a direct spectral integration technique (Oinas 1983) that is basically similar to the direct integration techniques developed by Kunde & Maguire (1974) and Scott (1974). We use a spectral resolution ($\Delta\nu$) of 0.5 cm^{-1} for the 180–900 and 1800–2300 cm^{-1} spectral intervals and 0.1 cm^{-1} for the 900–1200 cm^{-1} region. The 0.5 cm^{-1} spectral resolution that we use in the 5 μm region was found to be adequate by performing test calculations using much higher spectral resolution. For example, at the resolution of the IRIS observations (4.3 cm^{-1}) there is no significant difference between spectra calculated at 0.5 cm^{-1} and 0.1 cm^{-1} for the 1800–2300 cm^{-1} region of the spectrum since most of the radiation originates at pressures greater than 2 bars where the absorption lines are sufficiently pressure broadened.

The vertical structure of the atmosphere is divided into at least 60 "homogeneous" atmospheric layers (15 layers per decade of pressure) spanning the pressure range 0.001 to 20 bars. Since chemistry or condensation can modify the gas profiles, gas abundances are referenced to mixing ratios set in the deep atmosphere at 20 bars. Extra layer boundaries are inserted into the baseline vertical structure, coincident with thermochemically predicted cloud base locations (Carlson et al. 1987). As gas abundances are varied to fit the observed spectra, these cloud base levels are automatically adjusted in the model to maintain consistency. Hydrogen opacity is calculated using an algorithm supplied by B. J. Conrath (1986, private communication) which uses absorption coefficients based on the work of Birnbaum & Cohen (1976) and includes the temperature dependence based on the work of Bachet et al. (1983) and Dore, Nencini, & Birnbaum (1983). Contributions from H_2-He collisions are also included assuming a helium mole fraction of 0.12 (Gautier et al. 1981). For the remaining gases, line-by-line calculations are performed using the GSFC line atlas (G. L. Bjoraker 1987, private communication). For PH_3, we use the GEISA line atlas (Husson, Goldman, & Orton 1982) for the ν_1 and ν_3 bands and new line data for the $2\nu_2$, $\nu_2 + \nu_4$ and $2\nu_4$ (Tarrago et al. 1987). For CH_3D, we include both the ν_2 and $2\nu_6$ bands using the HITRAN data base (Rothman et al. 1987). For NH_3 we use the line data for the 1800–2100 cm^{-1} region (Lellouch et al. 1987). The line shapes are modeled using a Voigt profile (Pierluissi, Vanderwood, & Gomez 1977; Drayson 1975). To account for the sub-Lorentzian behavior of the far wings, we have adopted the common expedient of truncating the Lorentz profile 50 cm^{-1} from the center of each line. We have verified that this choice of a line cutoff does not affect our conclusions regarding gas abundances, provided that wing absorption extends beyond 10 cm^{-1}. We evaluate the absorption line coefficients at temperatures and pressures corresponding to model layer edges and assume a linear variation of the absorption coefficient strength between the upper and lower layer boundaries. In the case of hydrogen, the pressure-squared dependence of the absorption coefficient is explicitly included by means of weighting factors determined by the pressure-temperature layering structure of the model.

We avoid the use of isothermal layers by taking the temperature gradient within each atmospheric layer to be linear in the Planck function. This choice makes integration over the vertical extent of the atmosphere less critically dependent on the number of atmospheric layers. We have examined our results for models with 10 to 60 layers per decade of pressure; the adopted resolution is the minimum sufficient to model the spectral effects of the steep vertical gradient of water abundance in saturated conditions.

Our radiative transfer model also allows for the vertical variation of the para-hydrogen fraction with height (see Carlson, Lacis, & Rossow 1991c). The vertical distributions of the condensible species (NH_3 and H_2O) above their saturation levels in the troposphere are determined either by their saturation mixing ratios or by a specified relative humidity profile. The location of the saturation levels are determined by thermochemical equilibrium, given mixing ratios at 20 bars, using the chemistry model described by Carlson et al. (1987). In particular, the locations of the NH_3 and NH_4SH cloud bases depend on chemical reactions within and above the water cloud that vary with the ratios of NH_3 to H_2S and to H_2O. Since NH_3 and PH_3 are also photochemically reactive, the abundances of these gases are determined by vapor to gas scale height ratios above the NH_3 cloud base for NH_3 and above the 1 bar level for PH_3 (initially constrained to match the values determined by K82). The initial thermal profile, supplied by B. J. Conrath (1986, private communication), is iteratively adjusted until the synthetic and observed spectra agree to within the noise equivalent radiance at selected wavenumbers within the S(0) and S(1) lines of H_2 (285–610 cm^{-1}) in a manner similar to that presented in Smith (1970). A more detailed description of our radiative transfer model can be found in Carlson et al. (1991a).

2.2. *Abundance Profiles of the Trace Gases*

Since chemistry or condensation can modify the gas profiles, gas abundances are referenced to mixing ratios in the deep atmosphere. While we are primarily interested in the abundance and distribution of water vapor, we simultaneously retrieve vapor profiles for the other spectroscopically active species. Here we briefly summarize our results for the other trace species.

Of the gases in the Jovian atmosphere NH_3 has the most complicated vertical profile. In the deep atmosphere, i.e., below the water cloud, NH_3 is well-mixed with an abundance that is super solar ($\approx 4.45 \times 10^{-4}$). This value is larger than that found by K82 but in good agreement with the results of radio observations (e.g., de Pater & Massie 1985; Marten et al. 1980). Further, we find that the abundance of NH_3 must decrease in

the 1 to 2 bar region of the atmosphere consistent with the formation of NH_4SH cloud particles. A well-mixed abundance of 4.45×10^{-4} provides too much opacity in the 1800–1900 cm^{-1} spectral interval and an unacceptable fit to the far-infrared observations, but a solar abundance of NH_3 does not provide enough absorption in the 1800–1900 cm^{-1} interval. Thus, based on the difference in the location of the peak emission level between these two spectral regions, we conclude that the abundance of NH_3 must decrease in the 1–2 bar region. Further, the far-infrared observations suggest an abundance that is constant between 0.5 (NH_3 condensation level) and 1 bar and of order 10^{-5}. In particular, in the NEB hot spots we find that the NH_3 abundance in the region 0.5 to 1.0 bars is 3.0×10^{-5}. Above 0.5 bars, the NH_3 abundance is subsaturated with a profile very similar to that inferred by K82.

In the deep atmosphere, we find a PH_3 abundance of 6.0×10^{-7}. Above the 1 bar level the profile of PH_3 is spatially variable due to the combined effects of photochemistry and dynamics. However since our 5 μm analysis is not effected by this variability we refer the reader to the more detailed description of the PH_3 profile in Carlson et al. (1991a).

The well-mixed species such as CH_3D, GeH_4 and CO have the simplest distributions. We find that the IRIS observations are best-fit with a CH_3D abundance of 4.5×10^{-7}, consistent with the value determined by K82, though higher than that determined by BLK. The reason for this difference is that cloud absorption near 2200 cm^{-1} was overestimated by BLK due to the use of their absorbing cloud parameterization resulting in an underestimate of the CH_3D abundance. CO and GeH_4 have mole fractions of 1.0×10^{-9} and 7.0×10^{-10}, respectively. These values are consistent with the results of previous investigations (e.g., Bjoraker, Larson, & Kunde 1986b).

2.3. *Cloud Parameterization*

Thermochemical equilibrium models (e.g., Weidenschilling & Lewis 1973; Carlson et al. 1987) predict the formation of three cloud layers in the Jovian atmosphere. Starting from depth and assuming solar gas abundances, water condenses at 4.8 bars, followed by NH_4SH at 2.1 bars and NH_3 at 0.68 bars (Carlson et al. 1987). Figure 1 shows the spectral variation of particle single scattering albedos ($\tilde{\omega}_0$) for NH_3 ice, NH_4SH ice, and H_2O ice in the 5 μm region. The two curves shown for NH_3 are for small and large particle sizes (3 and 100 μm). A mixture of these particle sizes provides the best-fit to the IRIS observations in the 180–1200 cm^{-1} region. For the NH_4SH and H_2O clouds, it is not possible to obtain diagnostic particle size information since the spectral variation of $\tilde{\omega}_0$ across the 1800 to 2300 cm^{-1} interval, where the deeper clouds affect the radiation, is only weakly dependent on particle size. Hence, for these clouds, scattering properties are shown for a nominal size of 3 and 10 μm, respectively. (A different particle size assumption for the NH_4SH and H_2O clouds would result in a somewhat different phase function and would only require that the value of τ_{ref} be rescaled to maintain the same radiative extinction properties.) For all three condensates, the single scattering albedos are spectrally dependent (i.e., nongray) and significantly larger than zero which indicates that multiple scattering effects are important. From this standpoint alone, use of a single gray, nonscattering ($\tilde{\omega}_0 = 0$) cloud to represent the Jovian cloud structure is a poor approximation.

The spectral dependence of the cloud particle absorption and scattering is included using Mie theory. We use a gamma distribution (eq. [2.56] of Hansen & Travis 1974) to represent the particle size characteristics for a variety of values of the effective particle radius, a. We use the optical constants for NH_3 ice (Martonchik, Orton, & Appleby 1984), NH_4SH ice (G. Sill & J. Pearl 1988, private communication), water (Downing & Williams 1975), and water ice (Warren 1984) to determine the scattering and extinction efficiency factors, Q_{scat} and Q_{ext}, respectively. Model calculations are not particularly sensitive to the value of the effective variance of the particle size distribution provided that the distribution is sufficiently broad. In the above, we have generally used a gamma distribution with an effective variance, $b = 0.25$.

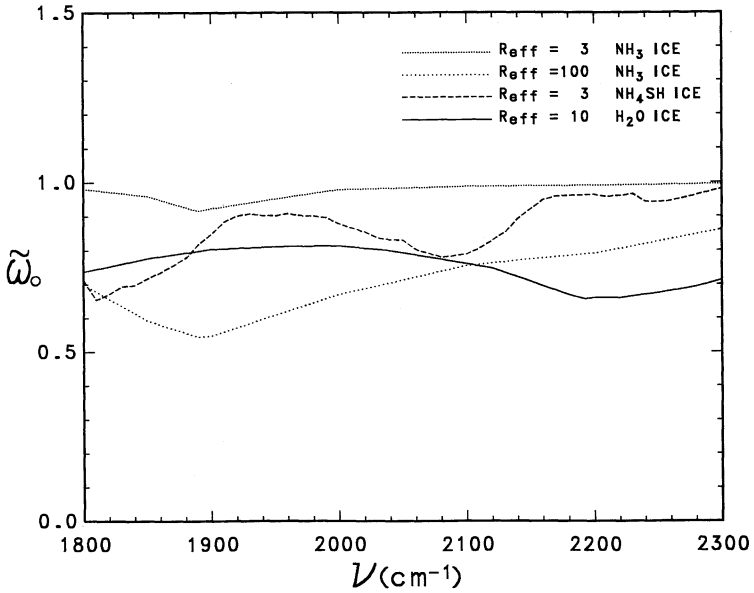

FIG. 1.—Particle single scattering albedos for NH_3 ice (*dotted lines*), NH_4SH ice (*dashed line*), and H_2O ice (*solid line*) as a function of wavelength for the 5 μm region. These single scattering albedos have been calculated for particle size distributions with effective radii of 3 and 100 μm for NH_3, 3 μm for NH_4SH and 10 μm for H_2O.

Cloud optical depth is specified as an extinction optical depth, τ_{ref}, at a reference wavelength ($\lambda = 0.5$ μm), where the Mie calculated extinction efficiency factor Q_{ext} is normalized to unity. Accordingly, at wavenumbers of interest, the monochromatic cloud optical depth is the product of τ_{ref} and the value of Q_{ext} at that particular wavenumber. At 5 μm, the unnormalized Q_{ext} values are typically about 2–3. The retrieved cloud parameters are the effective particle radius a and the optical depth referenced at 0.5 μm (τ_{ref}).

The vertical distribution of cloud opacity is modeled using a particle to gas scale height ratio, H_p/H_g, for each cloud. Extra layer boundaries are inserted into the model vertical structure to coincide with cloud base locations set by the pressure level of condensation. Thus, an individual cloud can physically extend through several layers in our model vertical structure and different clouds can physically overlap.

For multiple scattering calculations we use the doubling and adding method (Lacis & Hansen 1974). Self-emission from cloud particles as well as from the gas within the cloud is explicitly included in the calculations. Within each model layer, gaseous absorption and cloud extinction are taken to be uniformly mixed, i.e., within each layer, the single scattering albedo is specified as the ratio of the scattering optical depth to the extinction (absorption and scattering) optical depth within that layer.

For diagnostic purposes, we compute normalized cumulative contribution functions to determine the fractional contribution of each model layer to the total outgoing radiation at each wavelength. This yields the fractional ratios of the radiation emitted from a given pressure level in the atmosphere to the radiation emitted by the total atmosphere. Since the normalized contribution function includes the effects of atmospheric temperature on Planck emission as well as contributions from embedded cloud layers, it provides a more accurate determination of the peak emission level in the atmosphere than simply using the level where the clear gas absorption optical depth is unity, as in previous investigations (e.g., K82; BLK).

The model output is in the form of synthetic spectra covering the 180–2300 cm^{-1} spectral region which are convolved with the IRIS instrument function. The model also permits full access to the results of monochromatic calculations at any wavenumber.

A key feature of our investigation is that we model the full range of the IRIS data simultaneously, using the same radiative transfer model and atmospheric structure for all wavelengths. The far-infrared IRIS observations are required to constrain the temperature profile, the upper tropospheric gas composition, and the properties of the NH_3 cloud, whereas the 5 μm observations constrain the gas composition and cloud structure of the deeper atmosphere ($P > 2$ bars). The inclusion of the far-infrared observations in our analysis scheme allows for a more critically constrained and self-consistent investigation of the vertical distribution of the gas and particle opacity in the Jovian atmosphere than is possible with just the 5 μm observations. Although our discussion focuses on the 5 μm portion of the IRIS spectra, we stress that all results discussed fit the whole spectrum.

The model is structured to retain explicit (unparameterized) dependence on physical variables: thermal structure, gas abundances with variable profiles, cloud particle sizes, cloud optical depths, ratios of the particle to gas scale heights, and, in the case of photochemically reactive species (e.g., PH_3), a reference pressure above which the gas abundance falls off according to specified ratios of the "vapor" to gas scale height. For condensible species, the gas abundance profile above the condensation level follows either the saturation vapor pressure profile or a specified relative humidity profile. The relative humidity profile in the model is prescribed by a simplified vertical profile whereby the relative humidity can be specified at several pressures and linearly interpolated between them.

3. RESULTS

3.1. *Determination of the Water Abundance*

We constrain the Jovian thermal profile, the properties of the upper tropospheric NH_3 cloud, the abundance profiles of NH_3, PH_3, and CH_3D, and the vertical variation of the para-hydrogen fraction through an analysis of the far-infrared (180–1200 cm^{-1}) *Voyager* IRIS observations. The details of this retrieval process are presented in Carlson et al. (1991a). Figure 2 shows our best-fit (*solid line*) to the *Voyager* IRIS NEB hot spot observations in the 180–1200 cm^{-1} spectral interval. The averaged IRIS spectrum (*dotted line*) consists of the average of 52 individual IRIS spectra. To obtain a homogeneous sample, the emission angle is restricted to be less than 30°, with the average emission angle being $\approx$17°. The center of the IRIS field of view has been restricted to be within 7° to 13° N latitude with a spatial resolution of less than 5° of latitude. The highest spatial resolution in the sample is 0°.8 in latitude. Brightness temperature selection criteria further restrict the spectra to those with brightness temperatures larger than 149 K at 226 cm^{-1} and those with average brightness temperatures larger than 250 K over the 1950 to 2150 cm^{-1} spectral interval. The same brightness temperature and emission angle selection criteria were employed by K82 to define their hot spectral ensemble. Since radiation in the 200–1200 cm^{-1} interval originates at pressures less than 1.5 bars, the brightness temperature selection criterion at 226 cm^{-1} serves as a measure of the amount of NH_3 cloud opacity, with larger brightness temperatures associated with thinner NH_3 clouds. Similarly, high brightness temperatures in the 5 μm region (1950–2150 cm^{-1}) are indicative of an optically thin deep cloud structure. These brightness temperature selection criteria are thus used to select the hottest spectral ensemble and therefore the most transparent regions within the Jovian NEB.

The standard deviation of the individual IRIS spectra comprising the average is shown in the lower portion of Figure 2 (*coarser dotted line*). Most of this variation arises from real differences in atmospheric structure and from differences in emission angle and spatial resolution between the individual spectra. The difference between the synthetic spectrum and the ensemble average of the selected IRIS spectra is shown by the solid line in the lower portion of the figure. This difference is within the standard deviation of the IRIS spectra which serves as our criterion for a successful fit. The regions near 729 and 826 cm^{-1}, which contain stratospheric emission features due to acetylene and ethane, respectively, are not included as part of this analysis. These stratospheric emission features are localized to pressures well above the tropopause and do not affect the tropospheric retrieval, and, since they require a different modeling approach, they are deferred for a separate modeling investigation.

The NH_3 cloud in our best fit model consists of a mixture of 3 and 100 μm particles, with the large particles providing most of the cloud extinction. The total extinction optical depth of

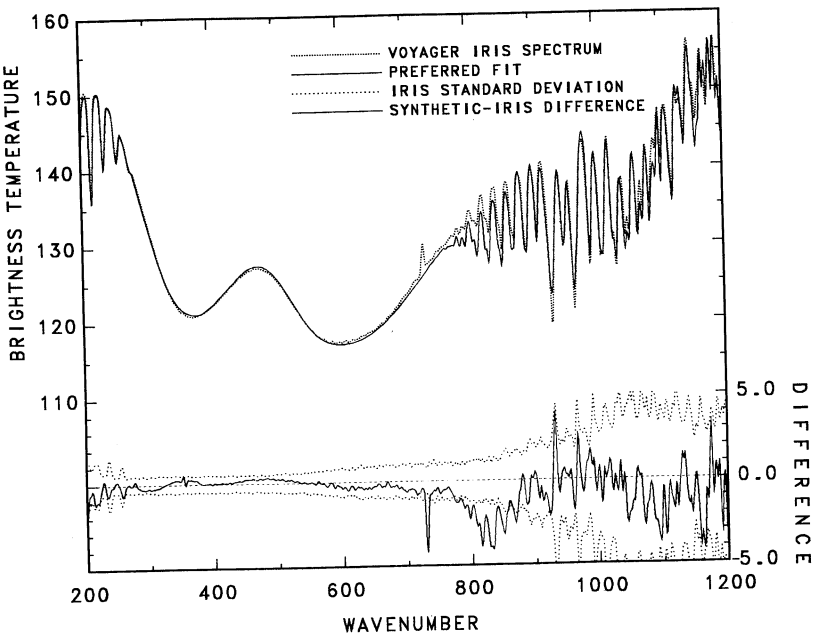

FIG. 2.—Comparison of the average IRIS NEB hot spot spectrum [NEB(hot), *dotted line*] and our best-fit synthetic spectrum (*solid line*) for the far-infrared (180–1200 cm^{-1}) region of the IRIS spectrum. The coarser dotted lines in the lower portion of the figure show the standard deviation of the individual IRIS spectra comprising the average. The difference between the synthetic and observed spectra is shown by the solid line near the bottom of the figure using the brightness temperature scale on the right-hand side. The stratospheric emission features due to C_2H_2 and C_2H_6 (729 and 826 cm^{-1}, respectively) have not been included in our calculations.

the NH_3 cloud is 0.27 (referenced at $\lambda = 0.5$ μm), with the large particles providing an optical depth of 0.19. The NH_3 cloud base is located at 0.5 bars with the NH_3 cloud particles vertically distributed with a particle to gas scale height ratio of 0.15. These NH_3 cloud properties are held fixed in all subsequent 5 μm calculations shown in this paper. The remaining structure in the difference spectrum in the 180–230 cm^{-1} region is attributable to the NH_3 vapor profile, where a more complex profile than that assumed would improve the agreement between the synthetic and observed spectra. A bimodal size distribution was found to be necessary in order to fit the spectral signature of the NH_3 cloud (Carlson et al. 1991a). Such bimodal size distributions are also characteristic of terrestrial cirrus clouds (e.g., Sassen, Starr, & Uttal 1989). The bimodal size distribution, per se, may be partly a modeling artifact because the commonly used size distributions are generally unable to describe (in a single distribution) the extremely broad range of particle sizes that appear to be characteristic of ice clouds.

Water vapor provides a dominant source of opacity in the 1900–2100 cm^{-1} spectral interval; so the abundance of water and its vertical distribution control the location of the peak emission level. Gaseous absorption from NH_3 also contributes significant opacity in the 1800–2000 cm^{-1} region, however, its abundance and vertical distribution have been previously determined from the analysis of the far-infrared observations and are thus held constant in all of these 5 μm calculations. To emphasize the range of pressures sampled in this wavelength interval and to illustrate the spectral dependence of water vapor absorption, we show in Figure 3 homogeneous path transmission spectra that are representative of water vapor absorption in the 2 bar region (average temperature 200 K and optical path length 10 cm atm, shown by the solid line) and in the 6 bar region (average temperature 300 K and optical path length 10^4 cm atm, shown by the dotted line). The larger optical path is representative of a nearly solar abundance of water. The point at which the optical depth of water vapor is unity corresponds roughly to the level where the cumulative contribution function has the value of 0.5. The influence of the water profile on this peak emission level is illustrated in Figure 4 which compares the peak emission level calculated for a 2 times solar abundance of water with a saturated (100% relative humidity) profile above the condensation level at 4.9 bars (*solid line*) and a well-mixed abundance of 3×10^{-5} corresponding to the value retrieved by K82 and BLK with a saturated water profile above the condensation level at 2.3 bars (*dotted line*). (Note that the contribution functions are computed line-by-line, but have been convolved with the IRIS instrument function and thus include some vertical overlapping between line core and line wing emission levels). The peak emission level, in Figure 4, includes both gaseous and NH_3 cloud opacity, but no H_2O cloud opacity. The assumed water profile dramatically changes the location of the peak emission level, with decreasing water abundance shifting the emission level to larger pressures. The water absorption features correspond to spikes in the peak emission level with the lines in the 1900 to 2000 cm^{-1} spectral region forming in the 2 to 4 bar region of the atmosphere.

It is important to remember that 50% of the emission originates below the level of peak emission. In the 3×10^{-5} water case, much of the continuum emission originates at pressures near to and larger than 5 bars. Thus, the arbitrary lower boundary imposed at 5 bars in the K82 analysis truncates the calculations, nonphysically restricting the computed emission to pressures less than 5 bars. This prompted the BLK reanalysis, which included a lower boundary at 12 bars, consistent with their assumption of a clear atmosphere at pressures greater than 2 bars.

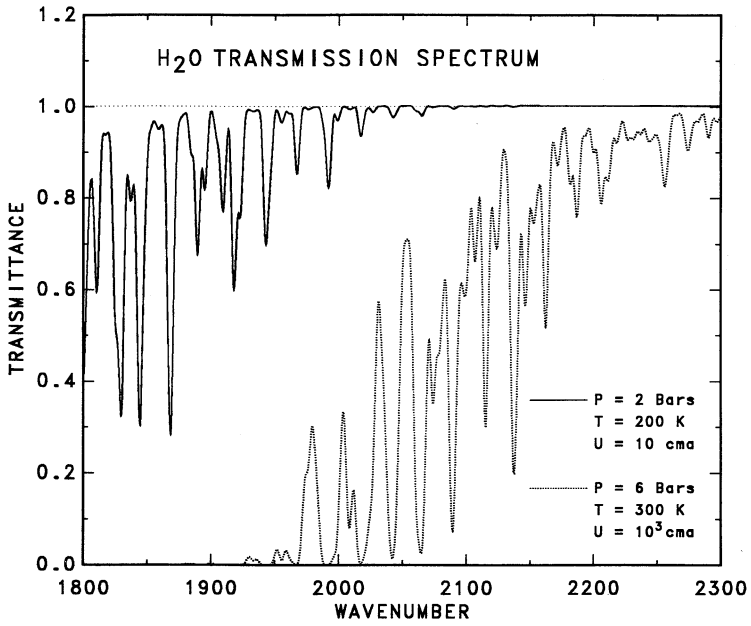

FIG. 3.—Synthetic homogeneous path transmission spectra for H_2O in the 1800 to 2300 cm^{-1} interval. The transmittances were calculated for (1) an average temperature of 200 K, average pressure of 2 bars and an optical path length of 10 cm atm (*solid line*) and (2) an average temperature of 300 K, average pressure of 6 bars and an optical path length of 10^4 cm atm (*dotted line*). These spectra contain the contribution from 5360 individual absorption lines and are plotted at the reduced 4.3 cm^{-1} resolution of the IRIS observations.

As noted by West, Strobel, & Tomasko (1986) and BLK, a nagging problem with the water profile retrieved by BLK is that there are no physical processes capable of reducing the mixing ratio from 3×10^{-5} at 6 bars to 4×10^{-6} at 4 bars, since the analysis explicitly assumes no clouds in this interval and the inferred water abundance is well below saturation throughout this region. Condensation appears to be the only reasonable candidate for producing such large abundance variations, since at this depth, photochemical reactions will not occur. Furthermore, chemical reactants would have to be nearly as abundant as H_2O in order to produce a significant depletion, but chemical models of the deep atmosphere which include all of the known gases with mixing ratios larger than 10^{-5} are unable to account for this depletion. Dynamics typically produces large-scale abundance variations of the order of a factor of a few but only above the condensation level (e.g., Rossow 1978).

Figure 5 shows a comparison between the average IRIS hot

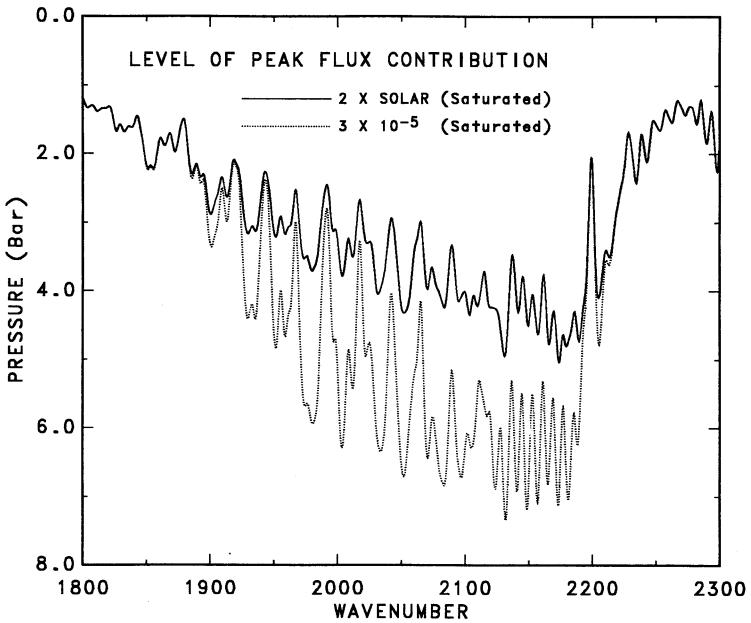

FIG. 4.—Effect of the water abundance on the peak emission pressure level. The solid line shows the location of the peak emission level calculated for a 2 times solar H_2O abundance, saturated water profile above 4.9 bars and no water cloud. The dotted line corresponds to a well-mixed water abundance of 3×10^{-5} and a saturated profile above 2.3 bars and no water cloud. Gaseous and NH_3 cloud opacity have been included in the calculation of the peak emission level.

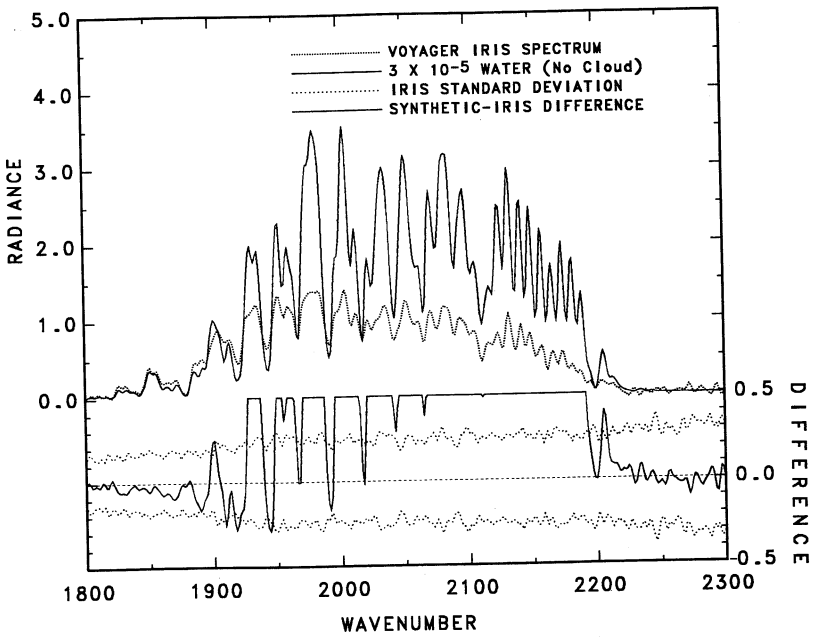

FIG. 5.—Comparison of the average 5 μm spectrum for IRIS NEB hot spots (*dotted line*) to a synthetic spectrum calculated with a well-mixed water abundance of 3×10^{-5} (*solid line*). Only NH_3 cloud opacity, consistent with longer wavelengths, has been included. These, and subsequent, spectra are plotted as radiances (in units of ergs s^{-1} cm^{-2} sr^{-1}/cm^{-1}). In the lower portion of the figure, the difference spectrum (truncated at the upper limit) shows that a significant amount of cloud opacity must be added to reduce the continuum level of the synthetic spectrum to match the IRIS observations.

spot spectrum (*dotted line*) and a synthetic spectrum (*solid line*) calculated for a well-mixed H_2O abundance of 3×10^{-5} with saturation occurring at 2.3 bars, but with no water cloud included there. NH_3 cloud opacity, constrained by the far-infrared analysis, has been included in this calculation. The large difference between the two spectra illustrates the dramatic effect that cloud opacity associated with the NH_4SH and H_2O clouds have on the synthetic spectrum. In the BLK and LDE analyses the effects of the NH_4SH and H_2O clouds were modeled as a single gray-absorbing cloud layer located near 2 bars. Therefore, this comparison is also illustrative of the effect that the gray absorbing cloud has on the synthetic spectrum since both BLK and LDE were able to fit the IRIS hot spot observations. The absorbing cloud in their analyses provided the additional opacity required to reduce the average level of the synthetic gas-only model spectrum to match that of the IRIS observations. However, the added cloud opacity in the 1900 to 2000 cm^{-1} region makes the fit worse, so BLK decreased the mixing ratio of water from 3×10^{-5} at 6 bars to 4×10^{-6} at 4 bars (in the line forming region, see Fig. 4). LDE deduced a well-mixed water abundance of $\approx 2 \times 10^{-6}$ from a fit to the spectrum in the 1900–2050 cm^{-1} region but with about twice the abundance of NH_3 as used by BLK. The extra NH_3 offsets the H_2O opacity in this spectral region.

Comparison of the BLK and LDE analyses also illustrates the point that the location of the absorbing cloud, 210 K in BLK versus 200 K in LDE, influences the retrieved water abundance. As will be discussed more fully later, the colder cloud at 200 K acts more like a neutral density filter, preserving line-to-continuum ratios better than the cloud at 210 K, because cloud self-emission is less from the colder cloud. The self-emission from the cloud at 210 K effectively provides fractionally less extinction in the center of the absorption features than the cloud at 200 K; thus, BLK required a slightly larger water abundance in the line-forming (2 to 4 bar) region than LDE in order to fit the IRIS observations. Therefore, with a gray absorbing cloud parameterization, the retrieved water profile is not really unique since it depends on the assumed temperature and location of the absorbing cloud.

Rather than parameterize the effect of NH_3, NH_4SH and H_2O clouds as a single grey absorbing cloud as in the K82, BLK, and LDE investigations, we use the optical constants for NH_3, NH_4SH and H_2O to include spectrally dependent absorption and emission. The substantial variation of the cloud particle single scattering albedo over the 1800–2300 cm^{-1} spectral interval (Fig. 1) also means that spectrally dependent scattering effects will be important. Moreover, gaseous absorption within these clouds introduces additional spectral dependence to the cloud extinction.

To avoid arbitrariness in the specification of cloud location and temperature, we use thermochemical equilibrium equations (Carlson et al. 1987) to determine the cloud base locations of each condensate given their abundances at 20 bars. Thus, in our analysis, the only variables for the condensible gases are their abundances at 20 bars and their relative humidities above the calculated saturation level. The cloud bases are always self-consistent with the chemical abundances of the condensible species. With a well-mixed water abundance of 3×10^{-5}, saturation occurs at 2.3 bars. The NH_4SH cloud forms at 1.9 bars. Thus, as noted by BLK, though not modeled as such, the 2 bar cloud in their analysis is a mixture of NH_4SH and H_2O cloud particles. Since NH_4SH and H_2O have single scattering albedos significantly larger than 0 (Fig. 1), multiple scattering effects are significant. Since the two clouds overlap above 1.9 bars, the cloud above 1.9 bars is a mixture of both NH_4SH and H_2O cloud particles and gas. Here, the single scattering albedo of the mixed composition cloud is determined as the ratio of the total scattering optical depth to the total extinction optical depth (gas and cloud) within the affected layers and the effective single scattering phase function

is the weighted mean with respect to the contributing scattering optical depths.

We include this spectral dependence of cloud extinction in Figure 6. Note the change in the radiance scale from Figure 5 to Figure 6. The vertical extent of both clouds is described by particle-to-gas scale height ratios which are constrained by the far-infrared observations to be 0.15 or less. A value of 0.15 has been used for these calculations. The optical depths of the NH_3, NH_4SH and H_2O clouds required to reduce the continuum level of the synthetic spectrum to the level observed are 0.27, 0.6, and 1.2, referenced at $\lambda = 0.5$ μm. It should be remembered that the optical depth of the NH_3 cloud was previously constrained through our analysis of the far-infrared observations. It is clear from this figure, that when *spectrally dependent* cloud extinction is included, a water mixing ratio of 3×10^{-5} cannot provide a satisfactory fit to the IRIS observations. In addition to the poor overall continuum fit, it is apparent that the water absorption features are too deep, implying that too much water is present in the line-forming region (2 to 4 bars). Decreasing the opacity of the water cloud would improve the spectral fit from 1850 to 1950 cm^{-1}, but would worsen the fit from 2000 to 2250 cm^{-1}. On the other hand, increasing the water cloud opacity would worsen the fit across the entire 5 μm window. Decreasing the water abundance, as in the LDE analysis, would improve the fit to the absorption features, but would worsen the fit to the overall continuum, requiring the inclusion of additional cloud opacity which would further worsen the fit of the synthetic spectrum to the IRIS observations.

Thus, inclusion of spectrally dependent cloud extinction in a manner that is consistent with the retrieved abundances of the condensible species precludes all subsolar solutions. Hence, the BLK result requires not only an explanation for the large change of H_2O abundance below the saturation level but also an explanation for the replacement of the NH_3, NH_4SH, and H_2O clouds with a single absorbing cloud located near 2 bars.

Figure 7 shows a comparison between the average IRIS hot spot spectrum (*dotted line*) and the synthetic spectra calculated with a 2 times solar abundance of water for a saturated (100% relative humidity) water profile above the base of the water cloud which forms at 4.9 bars. The solid line includes both NH_3 and water cloud opacity (with the optical depth of the water cloud selected to fit the continuum radiance level), while the dashed line includes NH_3 cloud opacity only. Clearly, neither of the synthetic spectra fit the observed spectrum, reconfirming the conclusion reached previously (e.g., BLK) that a saturated H_2O profile in the line-forming region, with or without clouds, cannot be correct.

The difference plot at the bottom of Figure 7, between the synthetic spectra calculated with and without water cloud opacity, delineates the spectral intervals where the water cloud affects the outgoing radiation, particularly in the window regions at 2130 and 2170 cm^{-1}. Based on the peak emission levels, shown previously in Figure 4, we know these spectral regions to be among the most transparent regions in the Jovian infrared spectrum with the peak emission level ocurring near 5 bars. Therefore it is not surprising that these spectral regions are particularly sensitive to the presence of the water cloud at this depth. Moreover, it is also clear that water cloud opacity is required in the spectral region near 2130 cm^{-1}, since the water vapor profile is already saturated near 5 bars and a further increase in water abundance would not provide the required opacity near 2130 cm^{-1}.

Apparently, BLK never considered a self-consistent solar abundance model. In all of their tabulated models, the only source of cloud opacity was their gray-absorbing cloud at 2 bars. Bjoraker (1985) did consider the influence of a gray-absorbing cloud at 5 bars on the synthetic spectrum, but,

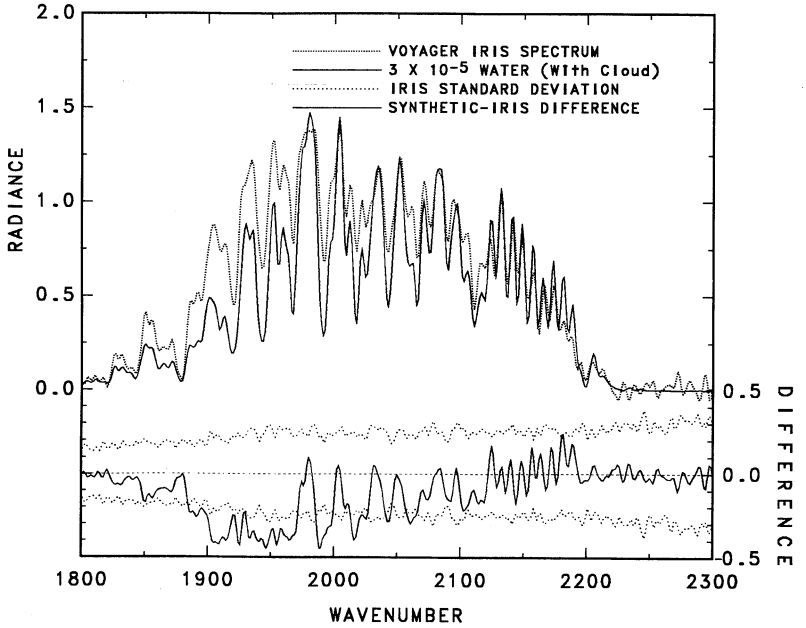

FIG. 6.—Same as Fig. 5, but with the inclusion of additional cloud opacity to provide the best-fit. Optical depths of the thermochemically consistent NH_3, NH_4SH and H_2O clouds are 0.27, 0.6, and 1.2, respectively (referenced at $\lambda = 0.5$ μm). The NH_4SH cloud base is at 1.9 bars and the H_2O cloud base is at 2.3 bars. Note also the change in the radiance scale relative to that in Fig. 5 (units are as in Fig. 5). The difference spectrum shows that subsolar water cannot provide an acceptable fit to the IRIS hot spot observations.

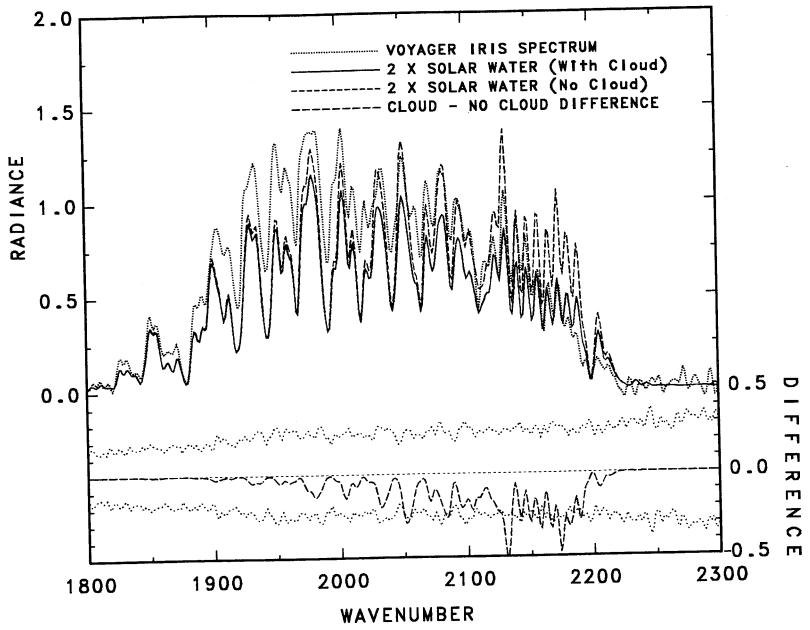

FIG. 7.—Comparison of the average IRIS hot spot spectrum (*dotted line*) to synthetic spectra for 2 times solar water calculated with (*solid line*) and without (*dashed line*) water cloud opacity. Scales are as in Fig. 6. Condensation occurs at 4.9 bars. A saturated (100% relative humidity) profile is assumed above the condensation level. The optical depth of the water cloud is 4. The difference spectrum in the lower portion of the figure shows the effect of water cloud opacity on the synthetic spectrum. The difference is taken between the synthetic spectrum calculated without and with water cloud opacity. Though water cloud opacity is clearly required to fit the IRIS observations in the 2100–2200 cm^{-1} spectral interval, a saturated water profile produces too much opacity in the 1900–2000 cm^{-1} region.

unfortunately, in these calculations, the assumed water profile was not consistent with the location of the cloud. Instead of using a solar or slightly supersolar abundance of water, which would have been consistent with a water cloud near 5 bars and a saturated water profile above the cloud base, Bjoraker (1985) used his depleted water profile. With the cloud opacity located at 5 bars, the cloud reduces the continuum level in the 2000 to 2250 cm^{-1} region where the radiation originates from pressure greater than 5 bars (Fig. 4), but has little effect on the 1900 to 2000 cm^{-1} region where the radiation originates from 2 to 4 bars, i.e., above the cloud. Superficially, the resulting synthetic spectrum resembled the IRIS observations from 2000 to 2250 cm^{-1} but from 1900 to 2000 cm^{-1} it resembled the synthetic spectrum in Figure 5. Thus, Bjoraker (1985) rejected a (solar water) cloud location at 5 bars based on his poor fit to the continuum near 1930 cm^{-1}. However, as shown in Figure 7, increasing the abundance of water can dramatically reduce the continuum level in the 1900 to 2000 cm^{-1} spectral interval.

The saturated water profile in Figure 7, with or without a water cloud at 5 bars, has too much opacity in the 1900–2000 cm^{-1} interval and cannot fit the IRIS observations. Yet, the opacity associated with a water cloud near 5 bars is required in order to fit the continuum near 2130 cm^{-1}. An obvious resolution of this dilemma is to reduce the relative humidity *above* the base of the water cloud and leave the well-mixed abundance of water unchanged at depth. This is clearly a physically more plausible way to reduce the amount of water in the line-forming region rather than attempting to deplete the well-mixed abundance of water below saturation. Accordingly, relative humidity above the condensation level should be considered as a retrievable physical parameter in the same sense as atmospheric temperature, composition, and cloud opacity.

Figure 8 shows a synthetic spectrum calculated with the same water abundance and cloud as shown in Figure 7 but with the relative humidity reduced to a mean value of 30% above the base of the water cloud. The optical depths of the NH_3, NH_4SH and H_2O clouds which optimize the fit to the IRIS spectrum are 0.27, 0.02 and 4.0, respectively. Thus, it is the water cloud and not the NH_4SH cloud that provides the bulk of the cloud opacity in NEB hot spots. Also, since the water cloud forms at a temperature of 283 K, well above the freezing point of water, the cloud forms in the liquid phase. A detailed discussion of spatial variations in NH_4SH cloud opacity can be found in Carlson et al. (1991a, b). The cloud particles are vertically distributed with particle to gas scale height ratios of 0.15. The resulting fit to the IRIS spectrum is everywhere within the IRIS standard deviation. Still, systematic deviations in continuum and line core regions that persist within the noise envelope suggest that greater structure exists in the relative humidity profile than has been assumed in the model fit.

The small optical depth retrieved for the NH_4SH cloud is consistent with the notion that NEB hot spots correspond to regions of minimum cloud opacity. Thus, Bézard et al. (1983) were able to use it as a proxy clear gas spectrum to study the influence of spatial variations in the optical depth of the NH_4SH cloud. However, the "clear" gas spectrum of Bézard et al. (1983) obviously contains the imbedded effect of the water cloud at 5 bars which reduces the window radiances at 2130 and 2170 cm^{-1} to their observed values. Finally, we note that the notion that the clouds in the Jovian atmosphere provide gray extinction is based on an interpretation of the ratio spectra shown in Figure 8 of Bézard et al. (1983), but it is clear from their ratio spectra that line-to-continuum ratios are not preserved and that a spectrally dependent slope is present in the ratios. The fact that these differences exist in the ratios of the different spectral ensembles is a definite indication that cloud opacity in the Jovian atmosphere is indeed nongray.

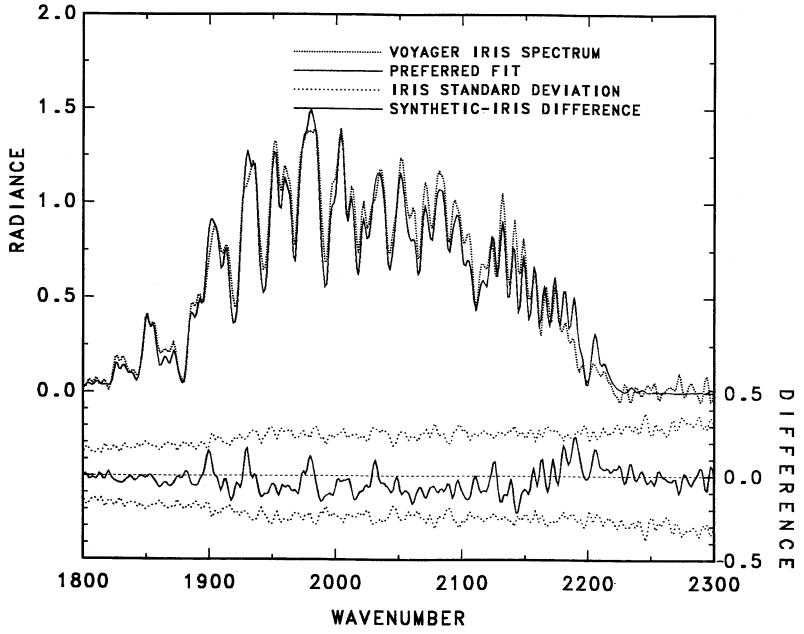

FIG. 8.—Comparison of the average IRIS hot spot spectrum (*dotted line*) to a synthetic spectrum calculated with a 2 times solar abundance of water and a reduced relative humidity profile above the cloud (*solid line*). Scales are as in Fig. 6. Optimum fit is obtained with the relative humidity decreasing from 100% at cloud base (4.9 bars) to 15% at 3 bars, then increasing to 100% at 1 bar, above which the relative humidity remains constant. The optical depths of the NH_3, NH_4SH, and H_2O clouds are 0.27, 0.02, and 4, respectively. This combination of parameters is our preferred fit to the entire IRIS spectrum for NEB hot spots.

The basis for trying a reduced relative humidity above the water cloud in the Jovian atmosphere is an analogy with the humidity structure observed in Earth's atmosphere: at low latitudes the relative humidity, even near the ocean surface, varies by 20% between upwelling and downwelling components of the Hadley circulation and decreases by more than 50% with altitude, even in the convective zone (Newell et al. 1972; Oort 1983). Strong dynamic downwelling over extensive low-level marine clouds in the subtropics causes a 50% depletion of relative humidity, even though cloud cover exceeds 60%. A study of drying effects by moist convection in the Jovian atmosphere by Del Genio & McGrattan (1990) also suggests that significant subsaturations are possible. The relative humidity profile used in this analysis is less complex than those decribed in Del Genio & McGrattan (1990) but qualitatively similar to their Figure 3*c*. In our model, the relative humidity of water gradually decreases from 100% at cloud base (4.9 bars) to a minimum of 15% at ≈ 3 bars and then increases again to 100% at 1 bar above which it remains constant with height. As shown in Figure 4, most of the 5 μm radiation originates well below the 1 bar level of the atmosphere, thus the IRIS 5 μm observations are not sensitive to the relative humidity profile above the 1 bar level. The relative humidity minimum near 3 bars, however, is required to provide the necessary "drying" effect on the synthetic spectrum due to the locations of the peak emission levels near this pressure level. Basically, the relative humidity profile has been retrieved in its simplest form. Some of the remaining structure of the difference plot, though within the standard deviation of the data, could no doubt be accounted for by using a more complex and spatially varying vertical profile. The fact that the relative humidity decreases above the base of the water cloud instead of above the model cloud top (as determined by the particle to gas scale height ratio) could imply either that there are multiple saturated and subsaturated layers above the initial condensation level (i.e., vertically layered clouds) or that within the IRIS field of view the water cloud is horizontally inhomogeneous (i.e., broken), both of which are characteristic of terrestrial water clouds. This explanation of the hot spot spectra is only viable if it is a local effect. In § 3.2 we discuss the spatial variability of relative humidity in the Jovian atmosphere.

Since water condenses in the Jovian atmosphere, it is only possible to determine a lower limit on the well-mixed water abundance from measurements of vapor abundance above the condensation level. Increasing the abundance of water merely shifts the base of the water cloud to higher pressures resulting in an increased continuum level, which can be easily compensated for by increasing the cloud opacity to match the 2130 cm^{-1} window radiance. Likewise, the relative humidity above the water cloud can be adjusted to match the observed line absorption in the 1900–2000 cm^{-1} region.

On the other hand, decreasing the water abundance to subsolar values shifts the base of the water cloud to lower pressures, where the spectral dependence of the water cloud extinction (especially when the cloud forms within the line-forming region, 2–4 bars) results in an unacceptably poor fit to the IRIS observations. Consequently, no synthetic spectrum calculated with subsolar water abundances and thermochemically consistent clouds is able to reproduce the observed continuum shape and the depth of the water absorption features. Even a solar abundance of water cannot simultaneously fit the line core and continuum radiances.

In Figure 9 we compare synthetic spectra calculated with well-mixed water abundances of 1.5, 2, and 10 times solar. In each case the NH_4SH and water cloud optical thicknesses and the water relative humidity have been readjusted to provide an optimum fit. The subtle differences between these spectra emphasize the point that we can only determine a lower limit to the well-mixed abundance of water in the Jovian atmosphere. The differences between our best-fit synthetic spectrum

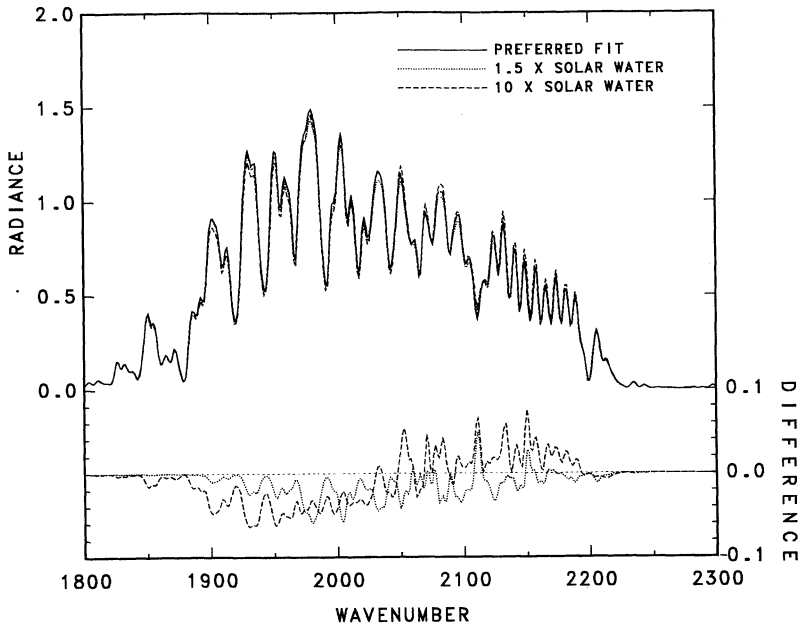

FIG. 9.—Comparison of our "best-fit" synthetic spectrum (*solid line*) with spectra calculated with water abundances that are 1.5 (*dotted line*) and 10 (*dashed line*) times solar. Scales are as in Fig. 6. The relative humidity profile for 1.5 times solar water is the same as that for our best-fit 2 times solar case (Fig. 8), but with saturation occurring at 4.6 bars. The optical depths of the NH_3, NH_4SH and H_2O clouds are 0.27, 0.02, and 3.3, respectively. A water abundance of 1.5 times solar corresponds to the lower limit to the actual water abundance on Jupiter. In the case of a 10 times solar abundance, the relative humidity of water remains 100% from cloud base (7.2 bars) to $\approx$4.6 bars above which it decreases to 15% at 3 bars and then increases to 100% at 1 bar, above which the relative humidity remains constant. In addition, in order to provide the requisite cloud opacity in the 5 bar region, the vertical extent of the water cloud has been increased consistent with the inferred humidity profile.

calculated with a 2 times solar abundance of water and those calculated with 1.5 and 10 times solar are shown in the lower portion of Figure 9.

For a 10 times solar abundance of water, the relative humidity of water remains 100% from cloud base (7.2 bars) to 4.6 bars above which it gradually decreases to a minimum of 15% at 3 bars. The relative humidity then increases to 100% at 1 bar, above this level the relative humidity remains constant. Thus, to fit the level of the continuum, water must remain saturated to $\approx$4.6 bars. The optical depths of the NH_3, NH_4SH, and H_2O clouds are 0.27, 0.05, and 10.0, respectively. However, for the H_2O cloud to provide the requisite opacity near 5 bars, the vertical extent of the water cloud must also be increased in the 10 times solar model by increasing the particle to gas scale height ratio to 0.25, consistent with the inferred relative humidity structure.

We emphasize that we can only determine a lower limit to the well-mixed abundance of water in the Jovian atmosphere, but that the minimum enhancement required to reproduce the IRIS observations is 1.5 times solar.

3.2. *Spatial Variations in Relative Humidity*

We selected NEB hot spots for our investigation of the abundance of water in the Jovian atmosphere because the low cloud opacity found in these regions provides the deepest penetration into the atmosphere. However, these regions cover only a small fraction of the planet. The bulk of the planet is represented by much colder spectral ensembles. *Voyager* IRIS observations of the whole NEB, reveal two distinct spectral categories based on 45 μm brightness temperature characteristics (Carlson et al. 1991a, b). One subset of the NEB observations, which contains the NEB hot spot spectral ensemble, consists of spectra with average 45 μm brightness temperatures in excess of 149 K [designated as NEB (hot) in Table 1]. Since radiation at far-infrared wavelengths originates above 1.5 bars, high 45 μm brightness temperatures are associated with regions of reduced NH_3 cloud opacity. The other NEB subset is comprised of observations with 45 μm brightness temperatures in the range 140 to 149 K. Thus, it is possible to define two spectral ensembles with the same 5 μm brightness temperature selection criterion but with different 45 μm brightness temperatures. In our analysis of NEB spectral ensembles (Carlson et al. 1991a, b), we found that spectra with average 45 μm brightness temperatures in excess of 149 K contain clouds that are relatively thin and that the cloud optical depth and water relative humidity increase with decreasing average 5 μm brightness temperatures. NEB spectra with average 45 μm brightness temperatures less than 149 K, have thicker clouds than their hot counterparts. Similarly, the colder 5 μm spectral ensembles are still fit by increasing the optical depth of the clouds as well as the relative humidity of water. In addition, we found that regardless of the average 45 μm brightness temperature, spectral ensembles with average 5 μm brightness temperatures less than 230 K are best-fit with a saturated water profile.

In our NEB analysis, one of our NEB spectral ensembles was defined by an average 45 μm brightness temperature between 140 and 149 K and an average 5 μm brightness temperature between 230 and 250 K [designated as NEB (warm) in Table 1]. Figure 10 shows a comparison of the average IRIS spectrum corresponding to this spectral ensemble and our best-fit synthetic spectrum. The IRIS spectrum (*dashed line*) is the average of 74 individual IRIS spectra with the cosine of the average emission angle equal to 0.957. In our best-fit spectrum (*solid line*) the optical depth of the NH_3 cloud is 0.50, with $\tau = 0.38$ provided by the large particles distributed according

TABLE 1

SUMMARY OF RETRIEVED CLOUD PARAMETERS

Parameter	NEB (hot)	NEB (warm)	EqZ (warm)	EqZ (cold)
Cloud Optical Depth				
NH_3 (large)	0.19 (0.15)[a]	0.38 (0.10)	0.40 (0.25)	0.55 (0.25)
NH_3 (small)	0.08 (0.15)	0.12 (0.15)	0.08 (0.15)	0.02 (0.15)
NH_4SH	0.02 (0.15)	0.45 (0.15)	0.95 (0.40)	1.80 (0.40)
H_2O	4.0 (0.15)	8.0 (0.15)	5.0 (0.15)	5.0 (0.35)
H_2O Relative Humidity				
2 bars (%)	30	20	20	100
3 bars (%)	15	70	70	100
Cloud-top para fraction				
f_p	0.32	0.32	0.33	0.34

[a] Values in parentheses are the particle-to-gas scale height ratios for the clouds.

to $H_p/H_g = 0.1$. The small particles are distributed with $H_p/H_g = 0.15$. The optical depth of the NH_4SH and H_2O clouds are 0.30 and 8.0, respectively, distributed with $H_p/H_g = 0.15$. The relative humidity of water is subsaturated above the water cloud with a minimum relative humidity of 20% at 2 bars.

It is possible to use the same brightness temperature selection criteria to define an Equatorial Zone spectral ensemble [designated EqZ (warm) in Table 1]. For this ensemble, the center of the IRIS field of view must lie between $\pm 3°$ latitude. Figure 11 shows a comparison of the average spectrum corresponding to this EqZ spectral ensemble and a synthetic spectrum calculated using the cloud and humidity structure retrieved for the NEB ensemble. The IRIS spectrum (*dashed line*) is the average of 70 individual spectra with the cosine of the average emission angle equal to 0.977. Our synthetic spectrum is shown (*solid line*). The difference between the synthetic and observed spectra is plotted in the lower portion of this figure. As can be seen, the difference is, for the most part, within the standard deviation of the individual spectra comprising the average. In other words, some regions of the EqZ have cloud opacities and relative humidities that are almost identical to some portions of the NEB. However, there are some characteristic differences. Additional NH_3 cloud opacity is required to improve the fit in the 200 to 300 cm^{-1} region, while more NH_3 cloud opacity is required at higher altitudes to improve the fit in the 400 to 520 cm^{-1} region. In addition, the continuum in the 950 to 1200 cm^{-1} region is poorly fit. In the 5 μm region, the 1800 to 2000 cm^{-1} interval is poorly fit, additional opacity is required in the 1 to 3 bar region of the atmosphere.

Figure 12 shows a comparison of our best-fit synthetic spectrum to this EqZ (warm) spectrum. The optical depth of the NH_3 cloud is 0.48 with $\tau = 0.4$ provided by the large particle distributed following $H_p/H_g = 0.25$. In this case, the NH_3 cloud extends from cloud base at 0.53 to 0.1 bars, instead of to 0.2 bars as in the NEB. The optical depth of the NH_4SH cloud is 0.95 distributed following a particle to gas scale height ratio of 0.4; thus while the bulk of the NH_4SH cloud opacity is distributed between 1.9 (cloud base) and 1.0 bars, some of the NH_4SH cloud particles are mixed upwards into the NH_3 cloud. The optical depth of the H_2O cloud is 5.0 distributed according to $H_p/H_g = 0.15$. Consistent with the results of Carlson et al. (1991c) and suggestive of a dynamical difference between belts and zones, we also find that the location of the para-hydrogen gradient is shifted to lower pressures. For this EqZ ensemble, we find that the parahydrogen gradient is located between 0.2 and 0.4 bars versus 0.2 and 0.5 bars in the NEB ensemble and that the para fraction increases from 0.25, the high-temperature equilibrium value, to 0.33.

In addition, the abundance of PH_3 above 1 bar is different. Since PH_3 is photochemically active in the Jovian atmosphere, the abundance of PH_3 falls off above 1 bar. We model this profile using a vapor to gas scale height ratio. In order to fit the continuum region near 980 cm^{-1} in our EqZ spectral ensemble, we have to increase the vapor to gas scale height ratio to 0.65 from our best-fit NEB value of 0.3, resulting in more PH_3 above the 1 bar level in the EqZ.

The relative humidity profile, however, is unchanged from that found in our NEB ensemble. The relative humidity decreases from 100% at cloud base (4.87 bars) to a minimum of 20% at 2 bars. Above this level the relative humidity increases to 100% at 1 bar. Thus, we find that even in a zone, if the average 5 μm brightness temperature is in excess of 230 K, the relative humidity of water is subsaturated in the line-forming 2–4 bar region of the atmosphere.

Regions with average 5 μm brightness temperatures less than 230 K are common on Jupiter. Figure 13 shows our best-fit to an EqZ spectral ensemble with an average 5 μm brightness temperature between 200 and 230 K [designated EqZ (cold) in Table 1]. The 45 μm brightness temperature is between 140 and 149 K. The IRIS spectrum (*dashed line*) consists of the average of 123 individual IRIS spectra with the cosine of the average emission angle equal to 0.975. Our best-fit synthetic spectrum (*solid line*) has an NH_3 cloud optical depth of 0.57 with $\tau = 0.55$ provided by the large particles distributed according to a particle to gas scale height ratio of 0.25. The optical depth of the NH_4SH cloud is 1.8 distributed according to a particle to gas scale height ratio of 0.4. Again NH_4SH cloud particles are mixed into the NH_3 cloud layer. The optical depth of the water cloud is 5.0 distributed according to $H_p/H_g = 0.35$. Consistent with the increased optical depth of the NH_3 cloud, we find that the cloud-top para fraction is 0.34. Again the vapor to gas scale height ratio controlling the PH_3 profile above 1 bar is 0.65.

The retrieved cloud parameters are summarized in Table 1 for the best-fit spectra presented in Figures 8, 10, 12, and 13. The selection criteria for the 5 μm brightness temperatures used to define the spectral ensembles are $T_B > 250$ K for the

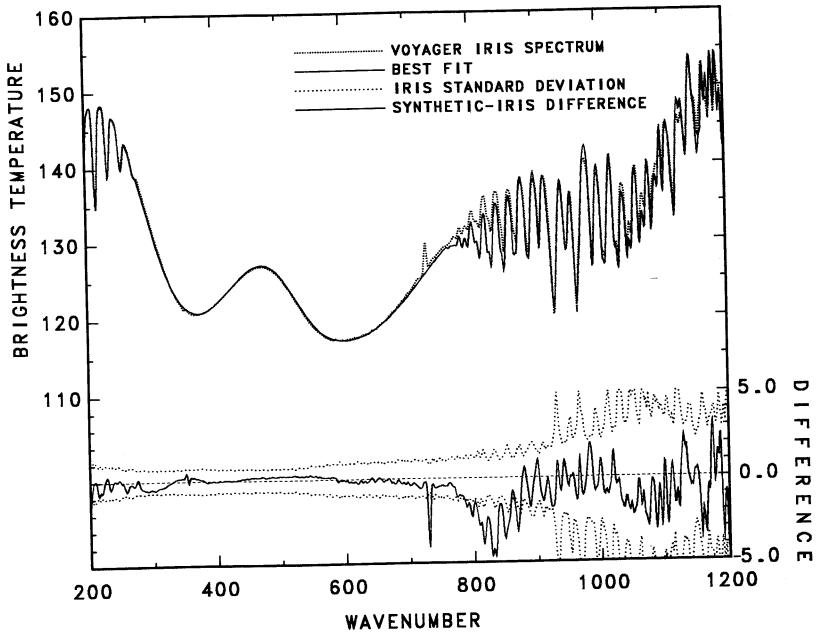

FIG. 10*a*

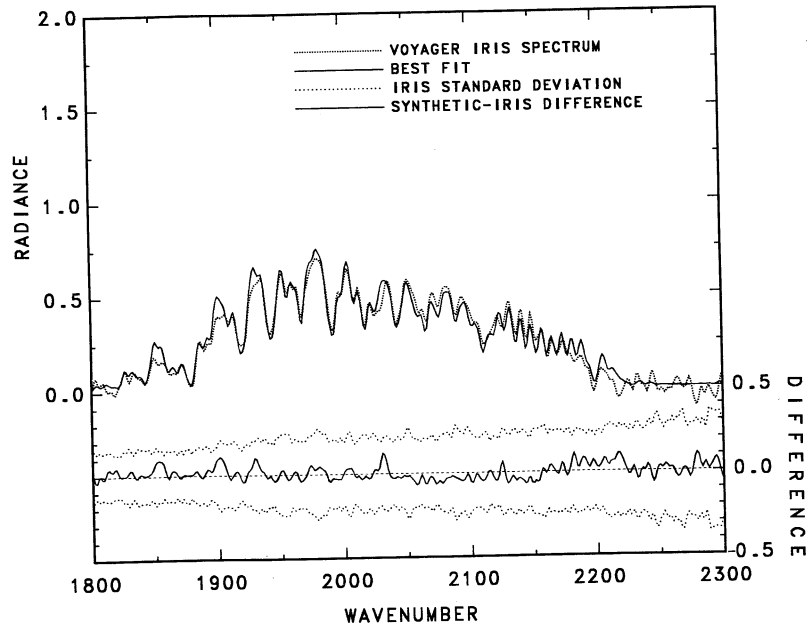

FIG. 10*b*

FIG. 10.—Comparison of the average IRIS spectrum (*dotted line*) corresponding to an intermediate NEB ensemble [NEB (warm)] and our best-fit synthetic spectrum (*solid line*) for the far-infrared (180–1200 cm^{-1}) region (Fig. 10*a*) and for the 5 μm (1800–2300 cm^{-1}) region (Fig. 10*b*; radiance is in units of ergs s^{-1} cm^{-2} sr^{-1}/cm^{-1}). The IRIS spectrum is the average of 74 spectra with 45 μm brightness temperatures between 140 and 149 K and average 5 μm brightness temperatures between 230 and 250 K. The average emission angle is 0.957. Our best-fit synthetic spectrum has cloud optical depths of 0.50, 0.45, and 8.0 for the NH_3, NH_4SH, and H_2O clouds, respectively. The relative humidity of water, above the water cloud, is subsaturated with the minimum relative humidity of 20% at 2 bars.

NEB hot spots, 230–250 K for the warm NEB and EqZ ensembles, and 200–230 K for the cold EqZ ensemble.

The increase in the amount of PH_3 aloft, the shift in the location of the para-hydrogen gradient to lower pressures, and the increased vertical extent of the clouds are all consistent with the presence of stronger upwelling motions. Thus, we would expect that if downwelling motions are responsible for the low relative humidities found in the hotter spectral ensembles that a more saturated humidity profile would provide the best-fit to this spectral ensemble and in fact that is the case. The humidity profile in Figure 13 remains saturated above the water cloud. To illustrate that a saturated profile does indeed provide the best-fit to the observations, we have calculated a synthetic spectrum using our hot spot relative humidity profile. Figure 14 shows a comparison between the IRIS EqZ (cold) spectrum (*dotted line*) and the synthetic spectrum calculated

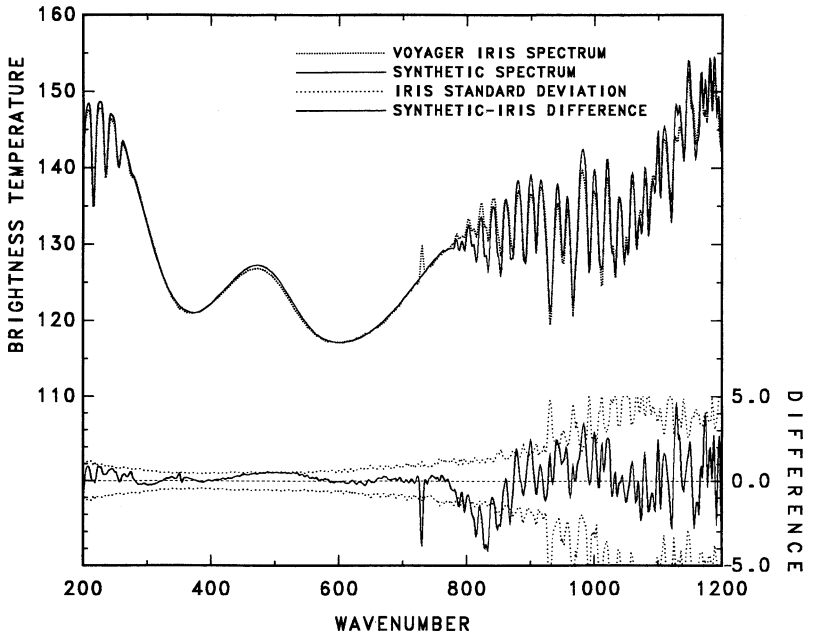

FIG. 11*a*

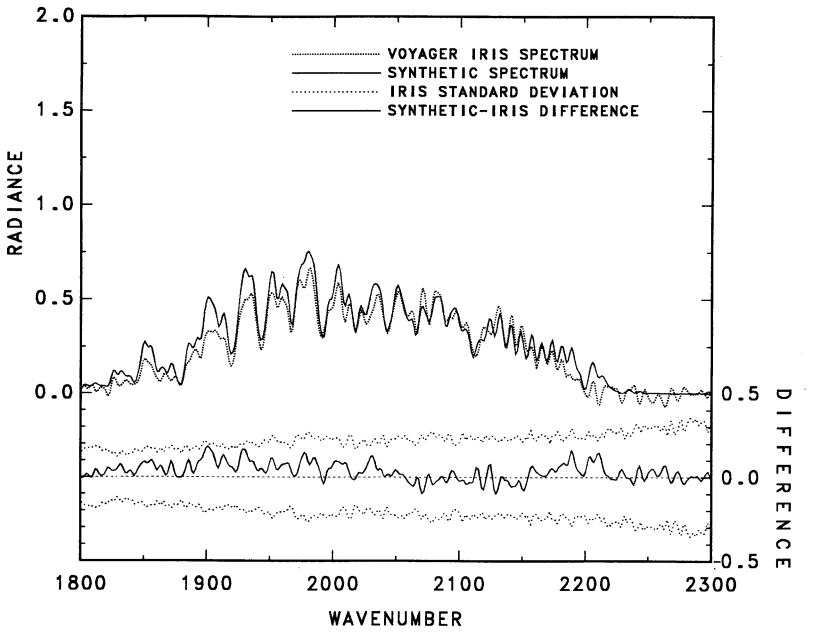

FIG. 11*b*

FIG. 11.—Comparison of the average IRIS spectrum (*dotted line*) corresponding to an Equatorial Zone spectral ensemble [EqZ (warm)] defined by the same brightness temperature selection criteria used to define the intermediate NEB ensemble in Fig. 10 and a synthetic spectrum (*solid line*) calculated using the same cloud and humidity structure retrieved for the intermediate NEB ensemble. The far-infrared (180–1200 cm^{-1}) region is shown in Fig. 11*a* and the 5 μm (1800–2300 cm^{-1}) region is shown in Fig. 11*b* (radiance is in units of ergs s^{-1} cm^{-2} sr^{-1}/cm^{-1}). The IRIS spectrum is the average of 70 spectra with an average emission angle of 0.977. The poor fit is indicative of small differences in cloud structure between belts and zones.

assuming a minimum relative humidity of 15% at 3 bars. The difference spectrum reveals that while this synthetic spectrum provides an acceptable fit to the IRIS observations in that the difference is less than the standard deviation of the individual spectra, the saturated water profile clearly minimizes the difference between the synthetic and observed spectra. Further, and perhaps more importantly, these figures indicate that a saturated water profile is consistent with these IRIS observations and cannot be ruled out.

4. DISCUSSION

Based on the results of our analysis, we conclude that the abundance of water on Jupiter must be *at least* 1.5 times solar. The precise abundance value cannot be uniquely determined

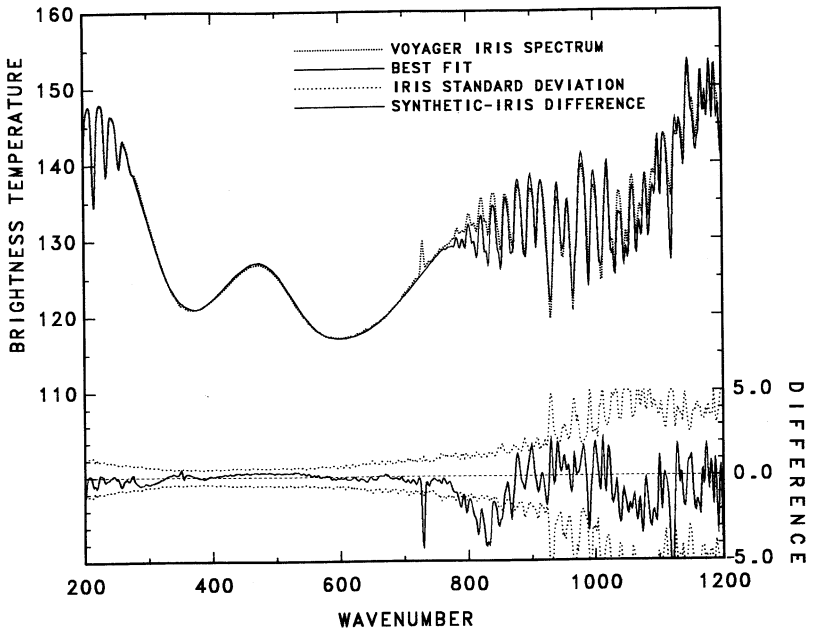

FIG. 12*a*

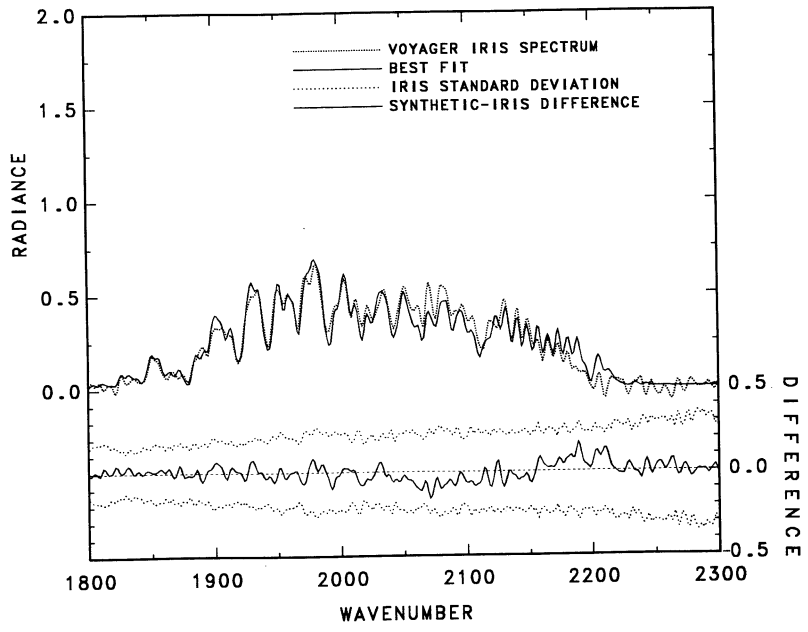

FIG. 12*b*

FIG. 12.—Comparison of the EqZ (warm) IRIS spectrum (*dotted line*) shown in Fig. 11 and our best-fit synthetic spectrum (*solid line*) for the far-infrared region (Fig. 12*a*) and the 5 μm region (Fig. 12*b*; radiance is in units of ergs s^{-1} cm^{-2} sr^{-1}/cm^{-1}). The synthetic spectrum has cloud optical depths of 0.48, 0.95, and 5.0 for the NH_3, NH_4SH, and H_2O clouds, respectively. In this case, NH_3 cloud opacity extends to lower pressure, following a particle to gas scale height ratio of 0.25, and the vertical extent of the NH_4SH cloud is similarly enhanced. The relative humidity profile, above the water cloud, is unchanged from that found in the intermediate NEB ensemble.

as was illustrated in Figure 9. In situ measurements made by the *Galileo* probe instruments below the water cloud ($P > 5$ bars) will be required to establish more precisely the value for the well-mixed abundance of water in the Jovian atmosphere. Nevertheless, we can firmly rule out subsolar abundances of water since they cannot provide a satisfactory fit to the IRIS observations when thermochemically self-consistent, spectrally dependent cloud extinction is included in models of the IRIS spectra. Supersolar water abundances provide the only acceptable fit to the IRIS observations with our preferred value being 2 times solar (2.76×10^{-3}).

This inferred enhancement of water, and hence oxygen, is also consistent with the range of enhancements previously determined for carbon and nitrogen. The CH_4 mixing ratio is fairly well constrained since CH_4 remains well-mixed throughout the Jovian atmosphere. The best current determination of

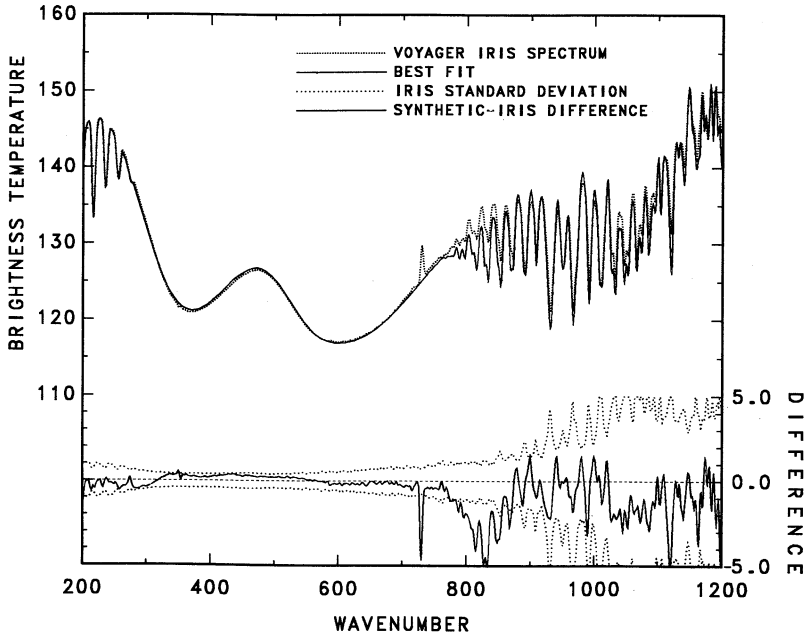

FIG. 13*a*

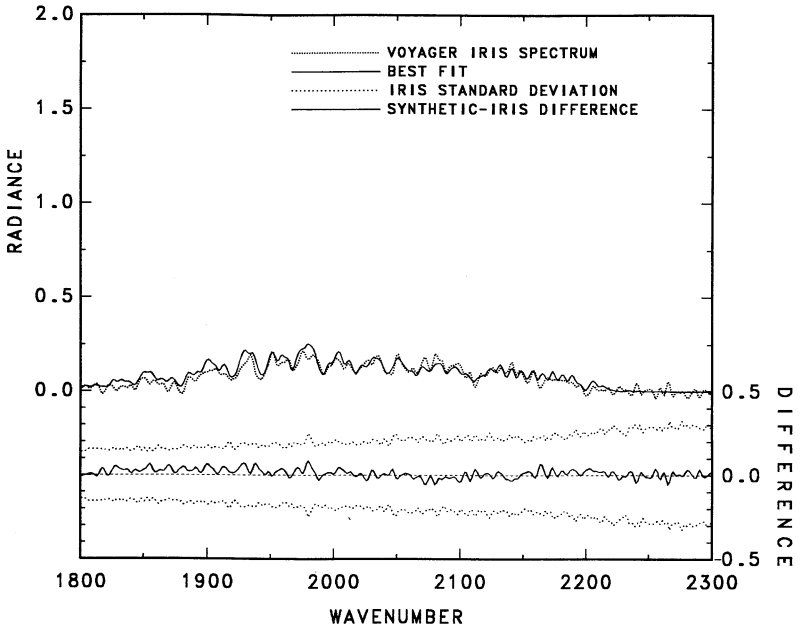

FIG. 13*b*

FIG. 13.—Comparison of the average IRIS spectrum (*dotted line*) corresponding to a colder Equatorial Zone ensemble [EqZ (cold)] than shown in Fig. 12 and our best-fit synthetic spectrum (*solid line*) for the far-infrared (Fig. 13*a*) and the 5 μm regions (Fig. 13*b*; radiance is in units of ergs s^{-1} cm^{-2} sr^{-1}/cm^{-1}). The IRIS spectrum is the average of 123 individual IRIS spectra with an average emission angle of 0.975. The 45 μm brightness temperatures are between 140 and 149 K, while the average 5 μm brightness temperatures are between 200 and 230 K. The synthetic spectrum has cloud optical depths of 0.57, 1.8, and 5.0 for the NH_3, NH_4SH, and H_2O clouds, respectively. All three clouds are vertically extensive with particle to gas scale height rations of 0.25, 0.40, and 0.35, respectively. The relative humidity of water is 100% above the water cloud.

the CH_4 abundance is $(2.18 \pm 0.18) \times 10^{-3}$ (Gautier & Owen 1983), which suggests that carbon is enhanced by a factor of ≈ 1.4 relative to the solar value. Recent determinations of the ammonia abundance on Jupiter reveal a broader spread due to the fact that NH_3 dissolves in water, reacts with H_2S to form NH_4SH, condenses, and is photochemically destroyed, all at different levels in the Jovian atmosphere. Recent determinations of the NH_3 abundance from analyses of the Jovian IRIS observations range from $(1.78 \pm 0.89) \times 10^{-4}$ by K82 to the value 4.8×10^{-4} retrieved by LDE from colder spectral ensembles within the NEB. These NH_3 abundances imply that nitrogen is enhanced by a factor of 1.0 to 2.7 times the solar value in the Jovian atmosphere. Our result for the deep atmosphere suggests an enhancement of roughly 2.5 times solar.

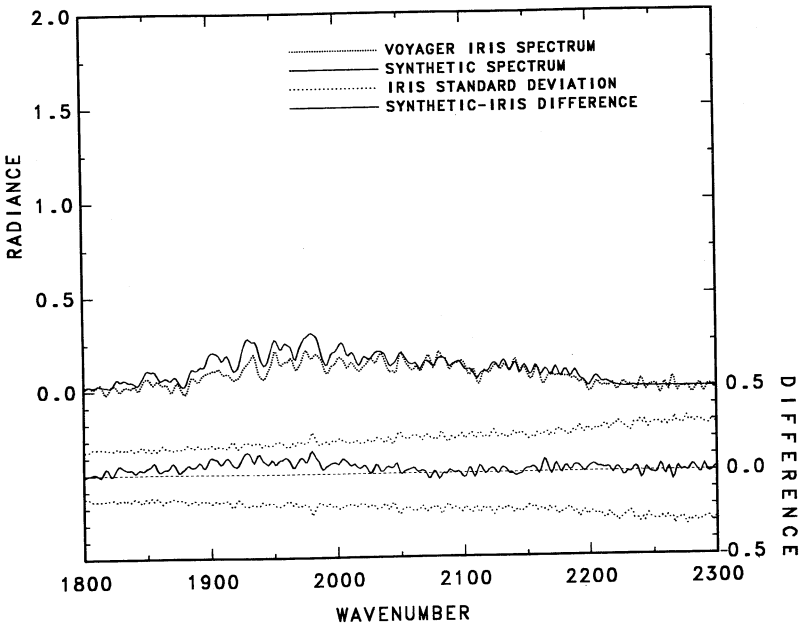

FIG. 14.—Comparison of the same average IRIS spectrum (*dotted line*) as shown in Fig. 13 and a synthetic spectrum (*solid line*) calculated assuming the retrieved NEB hot spot water humidity profile. Scales are as in Fig. 6. In this case the relative humidity is subsaturated above the water cloud with a minimum relative humidity of 15% at 3 bars. All other parameters are unchanged. The difference between the observed and synthetic spectra, plotted in the lower portion of the figure, reveals that, while a subsaturated humidity profile provides an acceptable fit to this ensemble, a saturated profile provides a better fit.

Our conclusion regarding the well-mixed abundance of water in the Jovian atmosphere is contrary to the conclusions of previous investigations. Nevertheless, we agree with the earlier findings that the mixing ratio of water is depleted (i.e., subsaturated) in the 2 to 4 bar region of the NEB hot spots. However, even within the NEB, there are areas where the relative humidity of water is saturated (see Carlson et al. 1991a, b). The magnitude of the spatial variations in relative humidity above the water condensation level between hot spots and colder spectral ensembles (e.g., zones) is sufficient to explain the results of Drossart & Encrenaz (1982), BLK, and LDE, which they interpreted as variations in the well-mixed abundance of water. We have shown that spectral ensembles with average 5 μm brightness temperatures in excess of 230 K are best-fit with a subsaturated water profile; conversely spectral ensembles with 5 μm brightness temperatures less than 230 K are best-fit with a saturated water profile. To illustrate the degree of spatial variability and the relationship between relative humidity, cloud opacity and dynamics, we show in Figure 15 a map of the average 5 μm brightness temperatures. The temperature

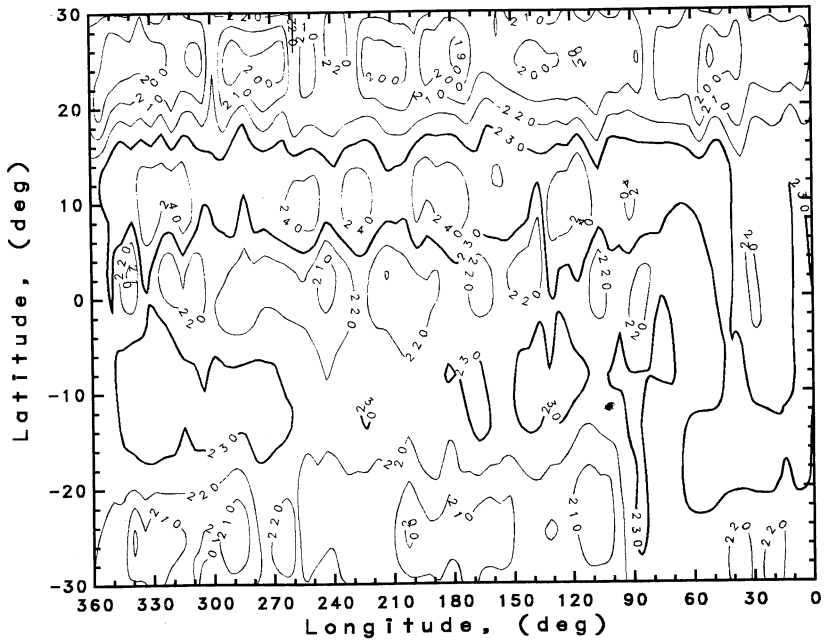

FIG. 15.—Map of the average 5 μm brightness temperatures observed by *Voyager* IRIS during the incoming mapping sequence. The emission angle is restricted to be less than 30°.

contours are in 10 K intervals. This map was constructed from the *Voyager* IRIS observations obtained during the incoming mapping sequence; thus the IRIS field of view is $\approx 10°$ latitude in diameter. We have chosen this subset, rather than the higher spatial resolution encounter observations which we have used for our analysis because of the more uniform longitudinal coverage. All of these observations have an emission angle less than 30°, corresponding to $\mu > 0.866$.

Regions with average 5 μm brightness temperatures in excess of 230 K are primarily found in the NEB and South Equatorial Belt (SEB, $-7°$ to $-13°$ latitude). Since belts are areas of predominantly downwelling motions, this is consistent with our notion that dynamic drying is responsible for the reduced relative humidities above the water cloud. As expected, zones have correspondingly colder brightness temperatures consistent with more saturated conditions. Thus, the primary difference between belts and zones is that zones contain more regions in which the relative humidity is saturated (i.e., colder spectra).

The Great Red Spot (GRS) is not apparent in this figure because its 5 μm brightness temperature is not significantly different from that of the South Tropical Zone (STrZ, -17 to $-23°$ latitude) in which it is located. In this figure, the GRS is located near 70° longitude between the two 230 K contours in the STrZ, suggesting that downwelling motions are found outside the GRS. This is consistent with the appearance of the GRS in the ground-based 5 μm image of Jupiter recorded on 1979 January 10 (see Fig. 3 of Terrile & Beebe 1979), in which the GRS is surrounded by warm areas.

The 5 μm brightness temperature map also reveals a number of localized brightness temperature minima and maxima which may be associated with wave motions in the Jovian atmosphere. While an analysis of these features is beyond the scope of this paper, it is important to note that similar features are observed in the 45 μm brightness temperature map shown in Figure 16. In this figure, the GRS is apparent as the 144 K brightness temperature minima near 70° longitude. The similarity in the overall appearance of these maps gives us greater confidence in our interpretation of our results. Again we see that regions with high 45 μm brightness temperatures, which are associated with optically thinner NH_3 clouds, are primarily found in belts. Zones, as expected, have lower 45 μm brightness temperatures corresponding to optically thicker NH_3 clouds. Note that the coldest 45 μm brightness temperatures are found in the NTrZ and STrZ where the 45 μm brightness temperature is typically of order 140 K. The coldest 45 μm brightness temperature found in the EqZ is 145 K. The difference in the observed 45 μm brightness temperatures between the tropical zones and equatorial zone is indicative of the differences in the cloud structure of these regions (see Carlson et al. 1991c).

Our analysis reveals a consistent relation between 5 and 45 μm brightness temperatures, cloud opacity, and water relative humidity. Areas of low 45 and 5 μm brightness temperatures correspond to regions of enhanced cloud opacity and high relative humidities and are associated with rising motions (i.e., zones), while areas of high 45 and 5 μm brightness temperatures correspond to regions of reduced cloud opacity and low relative humidities and are associated with downwelling motions (i.e., belts).

Our results strongly suggest that dynamic depletion of water vapor above the cloud-forming level occurs in the Jovian atmosphere as it does on Earth. The thinning of the NH_3 cloud and virtual disappearance of the NH_4SH cloud in hot spots is also consistent with "strong" dynamical downwelling motions that would be expected to reduce the relative humidity above the water cloud. Zones, which correspond to predominantly upwelling motions, are associated with higher relative humidities above the water cloud. However, even the lower limit to the water abundance on Jupiter implies that the cloud forms in the liquid phase, allowing for the occurrence of complex

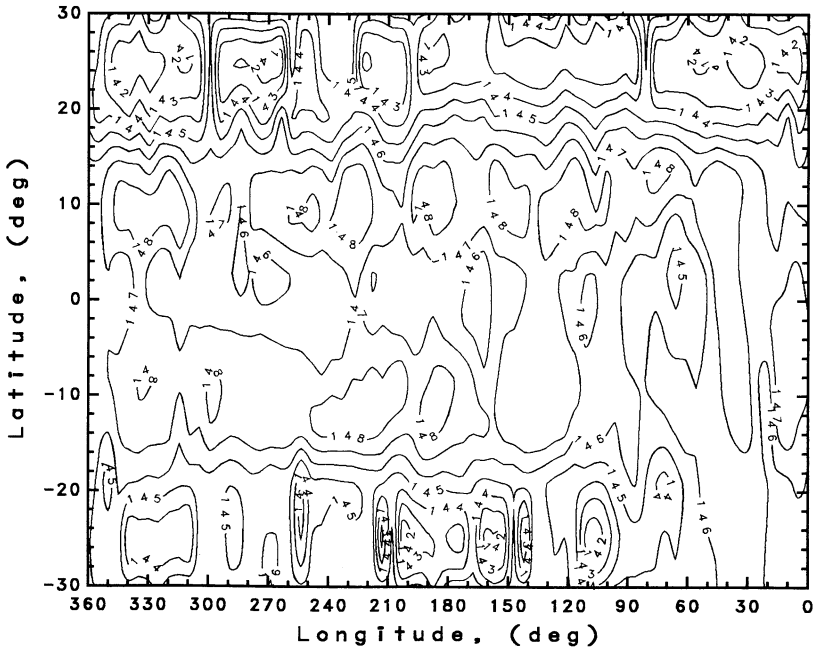

FIG. 16.—Corresponding map of the average 45 μm brightness temperatures observed by *Voyager* IRIS during the incoming mapping sequence. The emission angle is restricted to be less than 30°, restricting the areal coverage to $\pm 30°$ latitude.

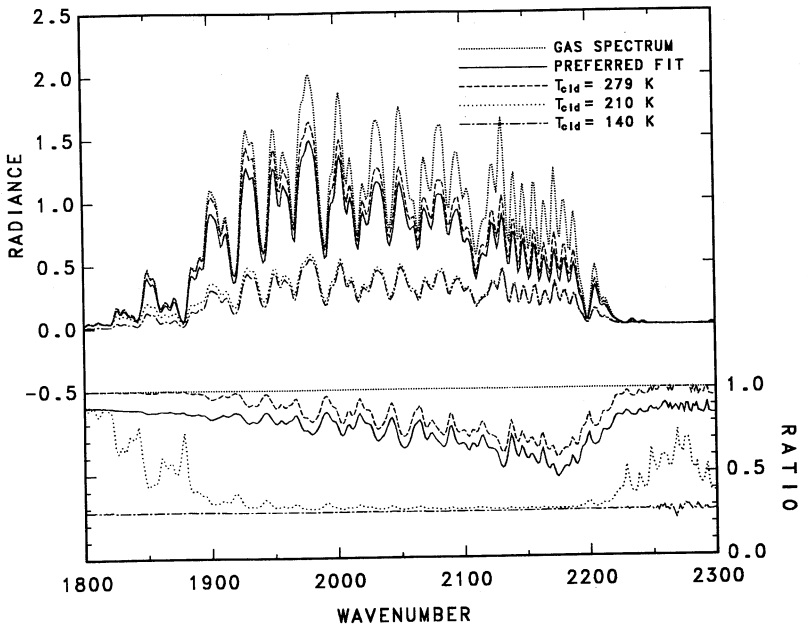

FIG. 17.—Effect of cloud self-emission on the continuum shape and the line-to-continuum ratios for an absorbing cloud parameterization. Radiance is in units of ergs s^{-1} cm^{-2} sr^{-1} cm. The synthetic spectra shown are the following: gas-only (*dotted line*), our best-fit nongray cloud model (*solid line*), gray-absorbing cloud at 279 K (*dashed line*), gray-absorbing cloud at 210 K (*broken line*) and gray-absorbing cloud at 140 K (*dash-dot line*). The lower portion of the figure shows the ratios of the cloud-containing spectra to the gas-only synthetic spectrum. A 2 times solar abundance of water and a reduced relative humidity profile have been used in all of these calculations.

(mixed-phase) microphysics above cloud base and a chemical coupling between the cloud layers in the Jovian atmosphere (see Carlson et al. 1987).

We conclude by noting that care must be exercised when simple "gray," absorbing cloud parameterizations are used. The spectral dependence of Planck emission from the gray cloud results in *nongray* extinction. This point is illustrated in Figure 17 which shows spectra calculated for a pure gas atmosphere (*dotted line*), our best-fit to the NEB hot spot observations (*solid line*), and an absorbing cloud of optical depth 1.24 at 279 K (*short dashes*), at 210 K (*long dashes*), and at 140 K (*dash-dot line*). The lower portion of Figure 17 shows ratios to the clear-gas spectrum for the synthetic spectra calculated with clouds. Purely gray extinction would correspond to a straight line. Our preferred model fit to the IRIS hot spot observations contains spectrally dependent cloud extinction and emission and results in a nongray ratio when compared to the clear gas spectrum. We note that a gray absorbing cloud located at 279 K provides an almost acceptable fit to the IRIS observations. Increasing the optical depth of the cloud would improve the fit. This is not surprising since the single scattering albedo of the water cloud is the ratio of the scattering optical depth to the total extinction optical depth, in-cloud water vapor absorption reduces the single scattering albedo of the water cloud to the point where the 2 times solar water cloud is nearly black. (This is not true of the water cloud near the 2 bar level when the BLK profile was considered, because the nearly two orders of magnitude variation in the water abundance from 2 times solar to 3×10^{-5} means that the extinction optical depth is much smaller for a reduced abundance of water and therefore the single-scattering albedo of the water cloud is much higher.) Furthermore, we can see that a gray absorbing cloud at 210 K results in nongray extinction. Because the cloud self-emission adds proportionately more to the absorption features than to the continuum regions, the cloud gives the appearance of providing more extinction in continuum regions than in the nearby absorption features. Such an effect distorts the line-to-continuum ratios used to retrieve gas abundances from spectra. Only a much colder absorbing cloud acts like a neutral density filter; thus for a cloud at 140 K the ratio is nearly a straight line.

Finally, we note that although the cold absorbing cloud preserves the line-to-continuum ratios of the gas-only spectrum, realistic clouds have spectrally dependent cloud extinction and self-emission that alters the line-to-continuum ratios. As a result, the gray approximation does not provide a reliable proxy for a more rigorous treatment of cloud extinction from the multilayer, radiatively interacting, cloud system in the Jovian atmosphere.

We thank R. Hanel and the *Voyager* IRIS team for designing such a capable instrument and obtaining one of the finest planetary data sets. We thank A. D. Del Genio, L. D. Travis, and M. Allison for many helpful discussions. We thank J. Ferrier, A. Wasilewski, and A. Wolf for programming support. We would like to acknowledge the support of the Planetary Atmospheres Discipline, NASA Office of Space Science and Applications.

REFERENCES

Allison, M. D. 1990, Icarus 83, 282
Bachet, G., Cohen, E. R., Dore, P., & Birnbaum, G. 1983, Canadian J. Phys., 61, 591
Bézard, B., Baluteau, J. P., & Marten, A. 1983, Icarus 54, 434
Birnbaum, G., & Cohen, E. R. 1976, Canadian J. Phys., 54, 593
Bjoraker, G. 1985, Ph. D. thesis, Univ. Arizona
Bjoraker, G. L., Larson, H. P., & Kunde, V. G. 1986a, ApJ, 311, 1058 (BLK)
———. 1986b, Icarus, 66, 579
Cameron, A. G. W. 1982, in Essays in Nuclear Astrophysics, ed. C. A. Barnes, D. D. Clayton, & D. N. Schramm (Cambridge: Cambridge Univ. Press), 23

Carlson, B. E., Lacis, A. A., & Rossow, W. B. 1992a, J. Geophys. Res., submitted
———. 1992b, J. Geophys. Res., submitted
———. 1992c, ApJ, in press
Carlson, B. E., Prather, M. J., & Rossow, W. B. 1987, ApJ, 322, 559
Del Genio, A. D., & McGrattan, K. B. 1990, Icarus, 84, 29
de Pater, I., & Massie, S. T. 1985, Icarus, 62, 143
Dore, P., Nencini, L., & Birnbaum, G. 1983, J. Quant. Spectros. Rad. Transf., 30, 245
Downing, H. D., & Williams, D. 1975, J. Geophys. Res., 80, 1656
Drayson, S. R. 1975, J. Quant. Spectros. Rad. Transf., 16, 611
Drossart, P., & Encrenaz, T. 1982, Icarus, 52, 483
Fegley, B., Jr., & Prinn, R. G. 1988, ApJ, 324, 621
Gautier, D., Conrath, B., Flasar, M., Hanel, R., Kunde, V., Chedin, A., & Scott, N. 1981, J. Geophys. Res., 86, 8713
Gautier, D., & Owen, T. 1983, Nature, 304, 691
Gierasch, P. J., Conrath, B. J., & Magalhães, J. A. 1986, Icarus, 67, 456
Hansen, J. E., & Travis, L. D. 1974, Space Sci. Rev., 16, 527
Hubbard, W. B., & Marley, M. S. 1989, Icarus, 78, 102
Husson, N., Goldman, A., & Orton, G. 1982, J. Quant. Spectros. Rad. Transf., 27, 501
Kunde, V., et al. 1982, ApJ, 263, 443 (K82)
Kunde, V. G., & Maguire, W. C. 1974, J. Quant. Spectros. Rad. Transf, 14, 803
Lacis, A. A., & Hansen, J. E. 1974, J. Atmos. Sci., 31, 118
Larson, H. P., Fink, U., Treffers, R. R., & Gautier, T. N. 1975, ApJ, 197, L137
Lellouch, E., Drossart, P., & Encrenaz, T. 1989, Icarus, 77, 457 (LDE)
Lellouch, E., Lacome, N., Guelachvili, G., Tarrago, G., & Encrenaz, T. 1987, J. Molec. Spectrosc., 124, 333
Marten, A., et al. 1981, Icarus, 46, 233
Marten, A., Courtin, R., Gautier, D., & Lacombes, A. 1980, Icarus, 41, 410
Martonchik, J. V., Orton, G. S., & Appleby, J. F. 1984, Appl. Opt., 23, 541
Newell, R. E., Kidson, J. W. Vincent, D. E., & Boer, G. J. 1972, The General Circulation of the Tropical Atmosphere and Interactions with Extratropical Latitudes, Vol. I, (Cambridge: MIT Press), 258
Noll, K. S., Knacke, R. F., Geballe, T. R., & Tokunaga, A. T. 1988, ApJ, 324, 1210
Oinas, V. 1983, J. Quant. Spectros. Rad. Transf., 29, 407
Oort, A. H. 1983, Global Atmospheric Circulation Statistics, 1958–1973, NOAA Professional Paper 14 (Rockville, MD: NOAA), 180
Pierluissi, J. H., Vanderwood, P. C., & Gomez, R. B. 1977, J. Quant. Spectros. Rad. Transf., 18, 555
Prinn, R. G., & Barshay, S. S. 1977, Science, 198, 1031
Rossow, W. B. 1978, Icarus, 36, 1
Rothman, L. S., et al. 1987, Appl. Opt., 26, 4058
Sassen, K., Starr, D. O'C., & Uttal, T. 1989, J. Atmos. Sci., 46, 371
Scott, N. A. 1974, J. Quant. Spectros. Rad. Transf., 14, 691
Smith, W. L. 1970, Appl. Optics, 9, 1993
Stevenson, D. J. 1982, Planet. Space Sci., 30, 755
Tarrago, G., Poussigue, G., Lacome, N., Lévy, A., & Guelachvili, G. 1987, in 42d Symposium on Molecular Spectroscopy (Columbus), Communications FB5 and FB6
Terrile, R. J., & Beebe, R. F. 1979, Science, 204, 948
Warren, S. G. 1984, Appl. Opt., 23, 1206
Weidenschilling, S. J., & Lewis, J. S. 1973, Icarus, 20, 465
West, R. A., Strobel, D. F., & Tomasko, M. G. 1986, Icarus, 65, 161